

A Color Elastica Model for Vector-Valued Image Regularization

Hao Liu ^{*} Xue-Cheng Tai [†] Ron Kimmel [‡] Roland Glowinski [§]

December 22, 2024

Abstract

Models related to the Euler's Elastica energy have proven to be very useful for many applications, including image processing and high energy physics. Extending the Elastica models to color images and multi-channel data is challenging, as numerical solvers for these geometric models are difficult to find. In the past, the Polyakov action from high energy physics has been successfully applied for color image processing. Like the single channel Euler's elastica model and the total variation (TV) models, measures that require high order derivatives could help when considering image formation models that minimize elastic properties, in one way or another. Here, we introduce an addition to the Polyakov action for color images that minimizes the color manifold curvature, that is computed by applying of the Laplace-Beltrami operator to the color image channels. When applied to gray scale images, while selecting appropriate scaling between space and color, the proposed model reduces to minimizing the Euler's Elastica operating on the image level sets. Finding a minimizer for the proposed nonlinear geometric model is the challenge we address in this paper. Specifically, we present an operator-splitting method to minimize the proposed functional. The nonlinearity is decoupled by introducing three vector-valued and matrix-valued variables. The problem is then converted into solving for the steady state of an associated initial-value problem. The initial-value problem is time-split into three fractional steps, such that each sub-problem has a closed form solution, or can be solved by fast algorithms. The efficiency, and robustness of the proposed method are demonstrated by systematic numerical experiments.

1 Introduction

The question of what is the appropriate metric when denoising/enhancing the quality of given images is fundamental in image processing and computer vision. In the literature, image regularization for grey-scale images has been extensively studied, of which one class of models takes advantage of the Euler elastica energy defined by [13, p.63]

$$E(v) = \int_{\Omega} \left(a + b \left| \nabla \cdot \frac{\nabla v}{|\nabla v|} \right|^2 \right) |\nabla v| d\mathbf{x}, \quad (1)$$

where $v : \Omega \rightarrow \mathbb{R}^+$ is a grey-scale image given as a function on a bounded domain $\Omega \subset \mathbb{R}^2$, $d\mathbf{x} = dx_1 dx_2$, with x_1, x_2 the coordinates of the generic point \mathbf{x} of Ω , while a and b are two positive scalar model parameters.

^{*}School of Mathematics, Georgia Institute of Technology, Atlanta, GA 30332, USA. Email: hao.liu@math.gatech.edu.

[†]Department of Mathematics, Hong Kong Baptist University, Kowloon Tong, Hong Kong. Email: xuecheng-tai@hkbu.edu.hk.

[‡]Computer Science Department, Technion, Haifa, Israel. Email: ron@cs.technion.ac.il.

[§]Department of Mathematics, University of Houston, Houston, TX 77204, USA. Email: roland@math.uh.edu, and Department of Mathematics, Hong Kong Baptist University, Kowloon Tong, Hong Kong.

Euler's Elastica has a wide range of uses in image processing, such as image denoising [14, 31, 38], image segmentation [2, 10, 37, 41], image inpainting [28, 31, 36], and image segmentation with depth [12, 22, 40], to name just a few. An important image denoising model, incorporating the Euler's Elastica energy, is

$$\min_v \int_{\Omega} \left(a + b \left| \nabla \cdot \frac{\nabla v}{|\nabla v|} \right|^2 \right) |\nabla v| d\mathbf{x} + \frac{1}{2} \int_{\Omega} |f - v|^2 d\mathbf{x}, \quad (2)$$

where $f : \Omega \rightarrow \mathbb{R}^+$ is the input image we would like to enhance and denoise. To find the minimizer of (2), one class of methods is based on the augmented Lagrangian method. In [31], an augmented Lagrangian method was proposed for image denoising, inpainting and zooming. Based on the method in [31], [11] suggested a fast augmented Lagrangian method and [38] proposed a linearized augmented Lagrangian method. A split-Bregman method was suggested in [36] to solve a linearized Elastica model introduced in [1]. Recently, an almost 'parameter free' operator-splitting method was presented in [8]; this method is efficient, robust, and has less parameters to adjust compared to augmented Lagrangian based methods.

A color image is a vector-valued signal represented by three RGB channels or four CMYK channels. While there are many papers and models that deal with greyscale image regularization, most of them can not be trivially extended to handle color images when taking the geometric properties of the color image into consideration. Inspired by an early paper [9] that focused on regularization functionals on vector-valued images, [27] proposed an anisotropic diffusion framework and [5] introduced a color TV norm for vector-valued images. A total curvature model was proposed in [32], in which the color TV term in [5] is replaced by summation over the curvatures of each channel. A generic anisotropic diffusion framework which unifies several PDE based methods was studied in [33]. The Beltrami framework was proposed in [29], it considers the image as a two-dimensional manifold embedded in a five-dimensional space-color (x, y, R, G, B) space. The image is regularized by minimizing the Polyakov action [23], a surface area related functional. Evolving the image according to the Euler-Lagrange equation of the functional gives rise to the Beltrami flow. To accelerate the convergence rate of the Beltrami flow, a fixed-point method was used in [3] and a vector-extrapolation method was explored in [24]. In [30], the authors used a short-time kernel of the Beltrami flow to smooth two-dimensional images on manifolds. Recently, a semi-implicit operator-splitting method [25] and an ALM based method [26] were proposed to minimize the Polyakov action for processing images. In [42], the authors used a primal-dual projection gradient method to solve a simplified Beltrami functional. A fidelity-Beltrami-sparsity model was proposed in [34], in which a sparsity penalty term was added to the Polyakov action. A generalized gradient operator for vector bundles was introduced in [4], which is applied in vector-valued image regularization. In [6], the Beltrami framework has been applied in active contour for image segmentation.

Recently, deep neural networks have been applied in image denoising. [20, 35] introduced BM3D [7] based convolutional neural networks in which each step of the celebrated BM3D algorithm is approximated by a convolutional neural network. A convolutional neural network based on a constrained minimization problem was proposed in [21] which can handle a wide range of noise levels using a single set of learned parameters. [39] proposed another convolutional network that can handle a wide range of noise levels and is able to handle spatially variant noise. Recently, total deep variation was introduced in [19] in which a convolution network extracting multi-scale local features is trained. This trained network serves as a regularizer in various kinds of image processing tasks without additional training. Although deep neural networks have demonstrated remarkable performance, the training methodology could limit the resulting filters to the set of observed examples. Moreover, one has to adjust the number of layers, filter sizes and learning rate. Empirical experience shows that deep networks with better representation ability are more difficult to train [17, 15]. Finally, when having an appropriate regularization model one could apply it as an additional loss, or as a standalone "unsupervised"

model.

The Polyakov action was shown to be a natural measure to construct selective smoothing filters for color images. To enrich the types of image formation models one could encounter, here, we propose a *color elastica* model which incorporates the Polyakov action and a Laplace-Beltrami term operating on the image channels, as a way to regularize color images. While the Polyakov action measures the area of the image manifold, the surface elastica can be computed by applying the Laplace-Beltrami operator on the color channels. It describes a second order geometric structure that allows for more flexibility of the color image manifold and could compensate the too restrictive area minimization. The new model is a natural extension of the Euler elastica model (2) to color images, which takes the geometrical relation between channels into account. Compared to the Polyakov action model, the suggested model is more challenging to minimize since the Laplace-Beltrami term involves high order nonlinear terms. Here, we use an operator-splitting method to find the minimizer of the proposed model. To decouple the non-linearity, three vector-valued and matrix-valued variables are introduced. Then, finding the minimizer of the proposed model can be shown to be equivalent to solving a time-dependent PDE system until the steady state is reached. The PDE system is time-discretized by the operator-splitting method such that each sub-problem can be solved efficiently. To the best of our knowledge, this is the first numerical method to solve the color elastica model. Unlike deep learning methods, the suggested model does not require training, though the model itself could be used as an unsupervised loss in general settings. Numerical experiments show that the proposed model is effective in selectively smoothing color images, while keeping sharp edges.

The rest of this paper is structured as follows: In Section 2, we briefly review the Polyakov action and the Beltrami framework. The color elastica model is introduced in Section 3. We derive the operator-splitting scheme in Section 4 and describe its finite difference discretization in Section 5. In Section 6, we demonstrate the efficiency, and robustness of the proposed method by systematic numerical experiments. We conclude the paper in Section 7.

2 The Polyakov action

In this section we briefly review the Riemannian geometry relevant to the Polyakov action as applied to color images. Since the Polyakov action is adopted from high energy physics, we temporally follow the Einstein’s summation notation convention in this section. We first introduce the metric on the Riemannian manifold. Denote a two-dimensional Riemannian manifold embedded in \mathbb{R}^d by Σ . Let (σ^1, σ^2) be a local coordinate system of Σ and $F(\sigma^1, \sigma^2) = (F^1(\sigma^1, \sigma^2), \dots, F^d(\sigma^1, \sigma^2))$ be the embedding of Σ into \mathbb{R}^d . Given a metric $\{g_{ij}\}$ for $i, j = 1, 2$, of Σ which is a symmetric positive definite matrix-valued metric tensor, the squared geodesic distance $(ds)^2$ on Σ between two points (σ^1, σ^2) and $(\sigma^1 + d\sigma^1, \sigma^2 + d\sigma^2)$ is defined by,

$$(ds)^2 = g_{\mu\nu} d\sigma^\mu d\sigma^\nu \equiv g_{11}(d\sigma^1)^2 + 2g_{12}d\sigma^1 d\sigma^2 + g_{22}(d\sigma^2)^2.$$

Assume F embeds Σ into a d -dimensional Riemannian manifold M with metric $\{h_{ij}\}$, $i, j = 1, \dots, d$. If $\{h_{ij}\}$ is known, we can deduce the metric of Σ by the pullback,

$$g_{ij}(\sigma^1, \sigma^2) = h_{\mu\nu} \partial_i F^\mu \partial_j F^\nu, \quad (3)$$

where ∂_i denotes the partial derivative with respect to the i^{th} coordinate, $\partial_i \equiv \partial/\partial\sigma^i$.

Consider a color image $\mathbf{f}(\sigma^1, \sigma^2) = (f_1, f_2, f_3)$ where (σ^1, σ^2) denote the spatial coordinates in the image domain, and f_1, f_2, f_3 denote the RGB color components. \mathbf{f} can be considered as a two-dimensional surface embedded in the five-dimensional space-feature space: $F = (\sqrt{\alpha}\sigma^1, \sqrt{\alpha}\sigma^2, f_1, f_2, f_3)$, where $\alpha > 0$ is a scalar parameter controlling the ratio between the space and color. Assuming the spacial and color spaces to be Euclidean, we have $h_{ij} = \delta_{ij}$ on

the space-feature space, where δ_{ij} is the Kronecker delta, $\delta_{ij} = 1$ if $i = j$ and $\delta_{ij} = 0$ otherwise. Set $\sigma^1 = x_1, \sigma^2 = x_2$. According to (3), the metric on the image manifold is

$$\mathbf{G} \equiv \{g_{ij}\} = \begin{pmatrix} \alpha + \sum_{k=1}^3 (\partial_1 f_k)^2 & \sum_{k=1}^3 \partial_1 f_k \partial_2 f_k \\ \sum_{k=1}^3 \partial_1 f_k \partial_2 f_k & \alpha + \sum_{k=1}^3 (\partial_2 f_k)^2 \end{pmatrix}. \quad (4)$$

Denote (Σ, g) the image manifold and its metric, and (M, h) its space-feature space and the metric on it. The weight of the mapping $F : \Sigma \rightarrow M$ is measured by

$$S(F, g_{ij}, h_{\mu\nu}) = \int d^m \sigma \sqrt{g} \|dF\|_{g,h}^2 \quad (5)$$

for $i, j = 1, \dots, \dim(\Sigma)$ and $\mu, \nu = 1, \dots, \dim(M)$, where $g = \det(\mathbf{G})$ and $\|dX\|_{g,h}^2 = \partial_i F^\mu \partial_j F^\nu g^{ij} h_{\mu\nu}$ with $F = (F^1, \dots, F^{\dim(M)})$ and $\{g^{ij}\}$ being the inverse of the image metric $\{g_{ij}\}$. With $m = 2, h_{ij} = \delta_{ij}$, the functional is known as the Polyakov action [23] in String Theory.

Substituting $h_{ij} = \delta_{ij}$ and (4) into (5) gives rise to

$$S(F) = \int \sqrt{g} d\mathbf{x} \quad \text{where } g = \det(\mathbf{G}). \quad (6)$$

Minimizing (6) by variational gradient descent, yields the Beltrami flow [18],

$$F_t^k = \frac{1}{\sqrt{g}} \nabla \cdot (\sqrt{g} \mathbf{G}^{-1} \nabla F^k), \quad (7)$$

where ∇F^k is a column vector by convention. The term on the right hand side of (7) is known as the Laplace-Beltrami operator applied to F^k .

Notations In the rest of the paper, we will use regular letters to denote scalar-valued functions, and bold letters to denote vector-valued and matrix-valued functions.

3 The formulation of the color elastica model

Let $\mathbf{f} = (f_1, \dots, f_d)^T$ be the given d dimensional signal to be smoothed, in which each component $f_k : \Omega \rightarrow \mathbb{R}^+$ represents a channel. Based on the Polyakov action (6), we define the color elastica model as,

$$\min_{\mathbf{v} \in V^d} \int_{\Omega} \left[1 + \beta \sum_{k=1}^d |\Delta_g v_k|^2 \right] \sqrt{g} d\mathbf{x} + \frac{1}{2\eta} \sum_{k=1}^d \int_{\Omega} |v_k - f_k|^2 d\mathbf{x}, \quad (8)$$

where $\mathbf{v} = (v_1, \dots, v_d)^T : \Omega \rightarrow \mathbb{R}^d$, Ω is the domain of f , V denotes the Soblev sapce $H^2(\Omega)$ on Ω , $\beta, \eta > 0$ are weight parameters. Similar to (4), let $\mathbf{G} = (g_{kr})_{1 \leq k, r \leq 2}$ be a symmetric positive-definite metric matrix depending on \mathbf{v} , where,

$$g_{11} = \alpha + \sum_{k=1}^d \left| \frac{\partial v_k}{\partial x_1} \right|^2, \quad g_{12} = g_{21} = \sum_{k=1}^d \frac{\partial v_k}{\partial x_1} \frac{\partial v_k}{\partial x_2}, \quad g_{22} = \alpha + \sum_{k=1}^d \left| \frac{\partial v_k}{\partial x_2} \right|^2,$$

for some $\alpha > 0$. We denote $g = \det \mathbf{G}$. Δ_g in (8) is the Laplace-Beltrami operator associated to \mathbf{G} ,

$$\Delta_g \phi = \frac{1}{\sqrt{g}} \nabla \cdot (\sqrt{g} \mathbf{G}^{-1} \nabla \phi), \quad \forall \phi \in V. \quad (9)$$

Here, we consider the case $d = 3$ for color images: $\mathbf{f} = (f_1, f_2, f_3)^T$ whose components represent the RGB channels. Then \mathbf{G} is the metric of the surface $F(x_1, x_2) = (\sqrt{\alpha} x_1, \sqrt{\alpha} x_2, v_1, v_2, v_3)$ induced by the denoised image \mathbf{v} and $g = \det \mathbf{G}$.

Remark 3.1. As described in Section 2, α represents the ratio between the spatial and feature coordinates. As α goes to 0, the ratio vanishes and the space-feature space reduces to the three-dimensional color space.

Remark 3.2. In the case f is a grey-scale image, dividing the first integral by $\sqrt{\alpha}$, model (8) reduces to

$$\begin{aligned}\tilde{E}_\alpha(v) \equiv & \int_{\Omega} \sqrt{\alpha + (v_x^2 + v_y^2)} d\mathbf{x} + \beta \int_{\Omega} \frac{1}{\sqrt{\alpha + (v_x^2 + v_y^2)}} \left(\nabla \cdot \frac{\nabla v}{\sqrt{\alpha + v_x^2 + v_y^2}} \right)^2 d\mathbf{x} \\ & + \frac{1}{2\eta} \int_{\Omega} |v - f|^2 d\mathbf{x}.\end{aligned}\quad (10)$$

As $\alpha \rightarrow 0$, (10) becomes

$$\tilde{E}_0(v) = \int_{\Omega} |\nabla v| d\mathbf{x} + \beta \int_{\Omega} \frac{1}{|\nabla v|} \left(\nabla \cdot \frac{\nabla v}{|\nabla v|} \right)^2 d\mathbf{x} + \frac{1}{2\eta} \int_{\Omega} |v - f|^2 d\mathbf{x} \quad (11)$$

which gives a variant of the elastica model (2), except that in (11) the weights depend on $|\nabla v|$. In other words, along the edges, the effect of the elastica term would be reduced.

The energy in (8) is highly nonlinear and is difficult to minimize. To simplify the nonlinearity, we introduce three vector-valued and matrix-valued variables. For $k = 1, 2, 3$ and $r = 1, 2$, let us denote by q_{kr} the real valued function $\frac{\partial v_k}{\partial x_r}$ and by \mathbf{q} the 3×2 matrix

$$\mathbf{q} = \begin{pmatrix} q_{11} & q_{12} \\ q_{21} & q_{22} \\ q_{31} & q_{32} \end{pmatrix} = \nabla \mathbf{v}.$$

Denote $\mathbf{q}_k = (q_{k1} \quad q_{k2})$, $k = 1, 2, 3$. We introduce the 3×2 matrix $\boldsymbol{\mu} = \sqrt{g} \mathbf{q} \mathbf{G}^{-1}$ with

$$\boldsymbol{\mu}_k = \sqrt{g} \mathbf{q}_k \mathbf{G}^{-1} \quad (12)$$

for each row of $\boldsymbol{\mu}$. We immediately have $\mathbf{q}_k = \frac{1}{\sqrt{g}} \boldsymbol{\mu}_k \mathbf{G}$. We shall use $\mathbf{M}(\mathbf{q})$ to be the matrix-valued function defined by

$$\mathbf{M}(\mathbf{q}) = \begin{pmatrix} \alpha + q_{11}^2 + q_{21}^2 + q_{31}^2 & q_{11}q_{12} + q_{21}q_{22} + q_{31}q_{32} \\ q_{11}q_{12} + q_{21}q_{22} + q_{31}q_{32} & \alpha + q_{12}^2 + q_{22}^2 + q_{32}^2 \end{pmatrix}, \quad (13)$$

and denote $\det \mathbf{M}(\mathbf{q})$ by $m(\mathbf{q})$, that is,

$$m(\mathbf{q}) = \det \mathbf{M}(\mathbf{q}).$$

Define $\mathbf{v}_\mathbf{q} = \{(v_\mathbf{q})_k\}_{k=1}^3$ to be the solution of

$$\begin{cases} \nabla^2(\mathbf{v}_\mathbf{q})_k = \nabla \cdot \mathbf{q}_k & \text{in } \Omega, \\ (\nabla(\mathbf{v}_\mathbf{q})_k - \mathbf{q}_k) \cdot \mathbf{n} = 0 & \text{on } \partial\Omega, \\ \int_{\Omega} (\mathbf{v}_\mathbf{q})_k dx = \int_{\Omega} f_k dx \\ \text{for } k = 1, 2, 3, \end{cases} \quad (14)$$

where \mathbf{n} denotes the unit outward normal along $\partial\Omega$. Define the sets Σ_f and S_p as

$$\Sigma_f = \left\{ \mathbf{q} \in (L^2(\Omega))^{3 \times 2}, \exists \mathbf{v} \in (H^1(\Omega))^3 \text{ such that } \mathbf{q} = \nabla v \text{ and } \int_{\Omega} (v_k - f_k) dx = 0 \text{ for } k = 1, 2, 3 \right\}, \quad (15)$$

$$S_\mathbf{G} = \{(\mathbf{q}, \boldsymbol{\mu}) \in ((L^2(\Omega))^{3 \times 2}, (L^2(\Omega))^{3 \times 2}), \boldsymbol{\mu}_k = \sqrt{g} \mathbf{q}_k \mathbf{G}^{-1}, k = 1, 2, 3 \text{ with } g = \det \mathbf{G}\} \quad (16)$$

and their corresponding indicator functions as

$$I_{\Sigma_f}(\mathbf{q}) = \begin{cases} 0, & \text{if } \mathbf{q} \in \Sigma_f, \\ \infty, & \text{otherwise,} \end{cases} \quad I_{S_{\mathbf{G}}}(\mathbf{q}, \boldsymbol{\mu}) = \begin{cases} 0, & \text{if } (\mathbf{q}, \boldsymbol{\mu}) \in S_{\mathbf{G}}, \\ \infty, & \text{otherwise.} \end{cases}$$

If $(\mathbf{p}, \boldsymbol{\lambda}, \mathbf{G})$ is the minimizer of the following energy

$$\begin{cases} \min_{\boldsymbol{\mu}, \mathbf{q}} \int_{\Omega} \left(\sqrt{g} + \frac{\beta}{\sqrt{g}} \sum_{k=1}^3 |\nabla \cdot \boldsymbol{\mu}_k|^2 \right) d\mathbf{x} + \frac{1}{2\eta} \sum_{k=1}^3 \int_{\Omega} |(\mathbf{v}_{\mathbf{q}})_k - f_k|^2 d\mathbf{x} + I_{\Sigma_f}(\mathbf{q}) + I_{S_{\mathbf{G}}}(\mathbf{q}, \boldsymbol{\mu}), \\ \mathbf{G} = \mathbf{M}(\mathbf{q}), \end{cases} \quad (17)$$

then \mathbf{v} solving (14) minimizes (8).

In (17), we rewrite the Laplace-Beltrami term as $\nabla \cdot \boldsymbol{\mu}_k$ where $\boldsymbol{\mu}$ linearly depends on \mathbf{q} . The metric $\sqrt{g} = \det \mathbf{M}(\mathbf{q})$ is also a function of \mathbf{q} . In the fidelity term, \mathbf{v} which solves (14) can be uniquely determined by \mathbf{q} . Thus the functional only depends on $\boldsymbol{\mu}$ and \mathbf{q} under some constraints on their relations. We then remove the constraints by incorporating the functional with the two indicator function $I_{\Sigma_f}(\mathbf{q})$ and $I_{S_{\mathbf{G}}}(\mathbf{q}, \boldsymbol{\mu})$. The resulting problem (17) is an unconstrained optimization problem with respect to $\boldsymbol{\mu}$ and \mathbf{q} only.

Remark 3.3. *Periodic boundary condition is a common condition in image processing. In this paper, we always assume the periodic boundary condition for $\mathbf{q}, \boldsymbol{\mu}, \mathbf{f}$ with Ω being a rectangle. Under this assumption, \mathbf{v} solving (14) also has the periodic boundary condition.*

4 Operator splitting method

In this section, we derive the operator-splitting scheme to solve (17).

4.1 Optimality condition

Denote

$$J_1(\mathbf{q}, \boldsymbol{\mu}, \mathbf{G}) = \int_{\Omega} \left(\sqrt{g} + \frac{\beta}{\sqrt{g}} \sum_{k=1}^3 |\nabla \cdot \boldsymbol{\mu}_k|^2 \right) d\mathbf{x}, \quad (18)$$

$$J_2(\mathbf{q}, \mathbf{G}) = \frac{1}{2\eta} \sum_{k=1}^3 \int_{\Omega} |(\mathbf{v}_{\mathbf{q}})_k - f_k|^2 d\mathbf{x} \quad (19)$$

with $g = \det \mathbf{G}$. If $(\mathbf{p}, \boldsymbol{\lambda}, \mathbf{G})$ is the minimizer of (17), it satisfies

$$\begin{cases} \partial_{\mathbf{q}} J_1(\mathbf{p}, \boldsymbol{\lambda}) + \partial_{\mathbf{q}} J_2(\mathbf{p}, \mathbf{F}) + \partial_{\mathbf{q}} I_{\Sigma_f}(\mathbf{p}) + \partial_{\mathbf{q}} I_{S_{\mathbf{p}}}(\mathbf{p}, \boldsymbol{\lambda}) \ni 0, \\ \partial_{\boldsymbol{\mu}} J_1(\mathbf{p}, \boldsymbol{\lambda}) + \partial_{\boldsymbol{\mu}} I_{S_{\mathbf{G}}}(\mathbf{p}, \boldsymbol{\lambda}) \ni 0, \\ \mathbf{G} - \mathbf{M}(\mathbf{p}) = 0, \end{cases} \quad (20)$$

where $\partial_{\mathbf{q}}$ denotes the partial derivative with respect to \mathbf{q} if its operand is a smooth function, and the sub-derivative if its operand is an indicator function. To solve (20), we introduce the artificial time and associate it with the initial value problem

$$\begin{cases} \frac{\partial \mathbf{p}}{\partial t} + \partial_{\mathbf{q}} J_1(\mathbf{p}, \boldsymbol{\lambda}, \mathbf{G}) + \partial_{\mathbf{q}} J_2(\mathbf{p}, \mathbf{G}) + \partial_{\mathbf{q}} I_{\Sigma_f}(\mathbf{p}) + \partial_{\mathbf{q}} I_{S_{\mathbf{G}}}(\mathbf{p}, \boldsymbol{\lambda}) \ni 0, \\ \gamma_1 \frac{\partial \boldsymbol{\lambda}}{\partial t} + \partial_{\boldsymbol{\mu}} J_1(\mathbf{p}, \boldsymbol{\lambda}) + \partial_{\boldsymbol{\mu}} I_{S_{\mathbf{G}}}(\mathbf{p}, \boldsymbol{\lambda}) \ni 0, \\ \frac{\partial \mathbf{G}}{\partial t} + \gamma_2 (\mathbf{G} - \mathbf{M}(\mathbf{p})) = 0, \\ (\mathbf{p}(0), \boldsymbol{\lambda}(0), \mathbf{G}(0)) = (\mathbf{p}^0, \boldsymbol{\lambda}^0, \mathbf{G}^0), \end{cases} \quad (21)$$

where $(\mathbf{p}^0, \boldsymbol{\lambda}^0, \mathbf{G}^0)$ is the initial condition which is supposed to be given, and γ_1, γ_2 are positive constants controlling the evolution speed of $\boldsymbol{\lambda}$ and \mathbf{G} , respectively. The choice of γ_1 will be discussed in Section 4.4.

4.2 Operator-splitting scheme

We use an operator-splitting method to time discretize (21). One simple choice is the Lie scheme [13]. We denote n as the iteration number, $\det \mathbf{G}^n$ by g^n , the time step by τ and set $t^n = n\tau$. Since $J_1(\mathbf{q}, \boldsymbol{\mu}, \mathbf{G})$ only contains g , when there is no ambiguity, we write $J_1(\mathbf{q}, \boldsymbol{\mu}, \mathbf{G})$ and $J_1(\mathbf{q}, \boldsymbol{\mu}, g)$ interchangeably. We update $\mathbf{p}, \boldsymbol{\lambda}, \mathbf{G}$ as follows,

Initialization

$$\text{Initialize } \mathbf{p}^0, \mathbf{G}^0, \boldsymbol{\lambda}^0 \text{ and compute } g^0 = \det \mathbf{G}^0. \quad (22)$$

Fractional step 1

Solve

$$\begin{cases} \frac{\partial \mathbf{p}}{\partial t} + \partial_{\mathbf{q}} J_1(\mathbf{p}, \boldsymbol{\lambda}, \mathbf{G}) + \partial_{\mathbf{q}} J_2(\mathbf{q}, \mathbf{G}) \ni \mathbf{0}, \\ \gamma_1 \frac{\partial \boldsymbol{\lambda}}{\partial t} + \partial_{\boldsymbol{\mu}} J_1(\mathbf{p}, \boldsymbol{\lambda}, \mathbf{G}) \ni \mathbf{0}, \\ \frac{\partial \mathbf{G}}{\partial t} + \frac{\gamma_2}{3}(\mathbf{G} - \mathbf{M}(\mathbf{p})) = \mathbf{0}, \\ (\mathbf{p}(t^n), \boldsymbol{\lambda}(t^n), \mathbf{G}(t^n)) = (\mathbf{p}^n, \boldsymbol{\lambda}^n, \mathbf{G}^n) \end{cases} \quad \text{in } \Omega \times (t^n, t^{n+1}), \quad (23)$$

and set $\mathbf{p}^{n+1/3} = \mathbf{p}(t^{n+1}), \boldsymbol{\lambda}^{n+1/3} = \boldsymbol{\lambda}(t^{n+1}), \mathbf{G}^{n+1/3} = \mathbf{G}(t^{n+1}), g^{n+1/3} = \det \mathbf{G}^{n+1/3}$.

Fractional step 2

Solve

$$\begin{cases} \frac{\partial \mathbf{p}}{\partial t} + \partial_{\mathbf{q}} I_{S_{\mathbf{G}^{n+1/3}}}(\mathbf{p}, \boldsymbol{\lambda}) \ni \mathbf{0}, \\ \gamma_1 \frac{\partial \boldsymbol{\lambda}}{\partial t} + \partial_{\boldsymbol{\mu}} I_{S_{\mathbf{G}^{n+1/3}}}(\mathbf{p}, \boldsymbol{\lambda}) \ni \mathbf{0}, \\ \frac{\partial \mathbf{G}}{\partial t} + \frac{\gamma_2}{3}(\mathbf{G} - \mathbf{M}(\mathbf{p})) = \mathbf{0} \\ (\mathbf{p}(t^n), \boldsymbol{\lambda}(t^n), \mathbf{G}(t^n)) = (\mathbf{p}^{n+1/3}, \boldsymbol{\lambda}^{n+1/3}, \mathbf{G}^{n+1/3}) \end{cases} \quad \text{in } \Omega \times (t^n, t^{n+1}), \quad (24)$$

and set $\mathbf{p}^{n+2/3} = \mathbf{p}(t^{n+1}), \boldsymbol{\lambda}^{n+2/3} = \boldsymbol{\lambda}(t^{n+1}), \mathbf{G}^{n+2/3} = \mathbf{G}(t^{n+1}), g^{n+2/3} = \det \mathbf{G}^{n+2/3}$.

Fractional step 3

Solve

$$\begin{cases} \frac{\partial \mathbf{p}}{\partial t} + \partial_{\mathbf{q}} I_{\Sigma_f}(\mathbf{p}, \boldsymbol{\lambda}) \ni \mathbf{0}, \\ \gamma_1 \frac{\partial \boldsymbol{\lambda}}{\partial t} = \mathbf{0}, \\ \frac{\partial \mathbf{G}}{\partial t} + \frac{\gamma_2}{3}(\mathbf{G} - \mathbf{M}(\mathbf{p})) = \mathbf{0} \\ (\mathbf{p}(t^n), \boldsymbol{\lambda}(t^n), \mathbf{G}(t^n)) = (\mathbf{p}^{n+2/3}, \boldsymbol{\lambda}^{n+2/3}, \mathbf{G}^{n+2/3}) \end{cases} \quad \text{in } \Omega \times (t^n, t^{n+1}), \quad (25)$$

and set $\mathbf{p}^{n+1} = \mathbf{p}(t^{n+1}), \boldsymbol{\lambda}^{n+1} = \boldsymbol{\lambda}(t^{n+1}), \mathbf{G}^{n+1} = \mathbf{G}(t^{n+1}), g^{n+1} = \det \mathbf{G}^{n+1}$.

Scheme (23)-(25) is only semi-discrete since we still need to solve the three sub-initial value problems. There is no difficulty in updating \mathbf{G} in (23)-(25) if $\mathbf{M}(\mathbf{p})$ is fixed, since we have the exact solution $\mathbf{G}(t^{n+1}) = e^{-\gamma_2 \tau/3} G(t^n) + (1 - e^{-\gamma_2 \tau/3}) M(\mathbf{p})$. To solve other subproblems, we suggest to use the Marchuk-Yanenko type discretization:

Initialize $\mathbf{p}^0, \mathbf{G}^0, \boldsymbol{\lambda}^0$ and compute $g^0 = \det \mathbf{G}^0$.

For $n \geq 0$, we update $(\mathbf{p}^n, \boldsymbol{\lambda}^n, \mathbf{G}^n, g^n) \rightarrow (\mathbf{p}^{n+1/3}, \boldsymbol{\lambda}^{n+1/3}, \mathbf{G}^{n+1/3}, g^{n+1/3})$

$\rightarrow (\mathbf{p}^{n+2/3}, \boldsymbol{\lambda}^{n+2/3}, \mathbf{G}^{n+2/3}, g^{n+2/3}) \rightarrow (\mathbf{p}^{n+1}, \boldsymbol{\lambda}^{n+1}, \mathbf{G}^{n+1}, g^{n+1})$ as:

$$\begin{cases} \frac{\mathbf{p}^{n+1/3} - \mathbf{p}^n}{\tau} + \partial_{\mathbf{q}} J_1(\mathbf{p}^{n+1/3}, \boldsymbol{\lambda}^n, m(\mathbf{p}^{n+1/3})) + \partial_{\mathbf{q}} J_2(\mathbf{p}^n, m(\mathbf{p}^{n+1/3})) \ni \mathbf{0}, \\ \mathbf{G}^{n+1/3} = e^{-\gamma_2 \tau/3} \mathbf{G}^n + (1 - e^{-\gamma_2 \tau/3}) \mathbf{M}(\mathbf{p}^{n+1/3}), \\ g^{n+1/3} = \det \mathbf{G}^{n+1/3}, \\ \frac{\boldsymbol{\lambda}^{n+1/3} - \boldsymbol{\lambda}^n}{\tau} + \partial_{\boldsymbol{\mu}} J_1(\mathbf{p}^{n+1/3}, \boldsymbol{\lambda}^{n+1/3}, g^{n+1/3}) \ni \mathbf{0}. \end{cases} \quad (26)$$

$$\begin{cases} \frac{\mathbf{p}^{n+2/3} - \mathbf{p}^{n+1/3}}{\tau} + \partial_{\mathbf{q}} I_{\mathbf{S}_{\mathbf{G}^{n+1/3}}}(\mathbf{p}^{n+2/3}, \boldsymbol{\lambda}^{n+2/3}) \ni \mathbf{0}, \\ \gamma_1 \frac{\boldsymbol{\lambda}^{n+2/3} - \boldsymbol{\lambda}^{n+1/3}}{\tau} + \partial_{\boldsymbol{\mu}} I_{\mathbf{S}_{\mathbf{G}^{n+1/3}}}(\mathbf{p}^{n+2/3}, \boldsymbol{\lambda}^{n+2/3}) \ni \mathbf{0}, \\ \mathbf{G}^{n+2/3} = e^{-\gamma_2 \tau/3} \mathbf{G}^{n+1/3} + (1 - e^{-\gamma_2 \tau/3}) \mathbf{M}(\mathbf{p}^{n+2/3}), \\ g^{n+2/3} = \det \mathbf{G}^{n+2/3}, \end{cases} \quad (27)$$

$$\begin{cases} \frac{\mathbf{p}^{n+1} - \mathbf{p}^{n+2/3}}{\tau} + \partial_{\mathbf{q}} I_{\Sigma_f}(\mathbf{p}, \boldsymbol{\lambda}) \ni \mathbf{0}, \\ \mathbf{G}^{n+1} = e^{-\gamma_2 \tau/3} \mathbf{G}^{n+2/3} + (1 - e^{-\gamma_2 \tau/3}) \mathbf{M}(\mathbf{p}^{n+1}), \\ g^{n+1} = \det \mathbf{G}^{n+1}, \\ \boldsymbol{\lambda}^{n+1} = \boldsymbol{\lambda}^{n+2/3}. \end{cases} \quad (28)$$

The discretization error depends on the value of τ ; it goes to 0 as $\tau \rightarrow 0$. In the following subsections, we discuss the solution of each of the sub-PDE systems (26)-(28).

4.3 On the solution of (26)

If $\mathbf{p}^{n+1/3}$ is the minimizer of the following problem, then the Euler-Lagrangian equation for it is exactly (26) and this means $\mathbf{p}^{n+1/3}$ solves (26):

$$\begin{aligned} \mathbf{p}^{n+1/3} = \arg \min_{\mathbf{q} \in (L^2(\Omega))^{3 \times 2}} & \left[\frac{1}{2\tau} \int_{\Omega} |\mathbf{q} - \mathbf{p}^n|^2 dx \right. \\ & \left. + \int_{\Omega} \left(\sqrt{m(\mathbf{q})} + \frac{\beta}{\sqrt{m(\mathbf{q})}} \sum_{k=1}^3 |\nabla \cdot \boldsymbol{\lambda}_k^n|^2 \right) d\mathbf{x} \right]. \end{aligned} \quad (29)$$

This problem can be solved by the Newton's method. The functional in (29) is in the form of

$$E_1 = \frac{1}{2\tau} \int_{\Omega} |\mathbf{q} - \mathbf{p}|^2 dx + \int_{\Omega} \left(s_1 \sqrt{m(\mathbf{q})} + \frac{\beta s_2}{\sqrt{m(\mathbf{q})}} \right) d\mathbf{x} \quad (30)$$

for some $s_1, s_2 \geq 0, \mathbf{p} \in (L^2(\Omega))^{3 \times 2}$. The first and second order variation of E_1 with respect to $q_{kr}, k = 1, 2, r = 1, 2, 3$ are

$$\frac{\partial E_1}{\partial q_{kr}}(\mathbf{q}, \mathbf{p}) = \frac{1}{\tau} (q_{kr} - p_{kr}) + \frac{1}{2} \left(s_1 (m(\mathbf{q}))^{-\frac{1}{2}} - \beta s_2 (m(\mathbf{q}))^{-\frac{3}{2}} \right) \frac{\partial m(\mathbf{q})}{\partial q_{kr}}, \quad (31)$$

$$\begin{aligned} \frac{\partial^2 E_1}{\partial q_{kr}^2}(\mathbf{q}, \mathbf{p}) = & \frac{1}{\tau} + \frac{1}{2} \left(s_1 (m(\mathbf{q}))^{-\frac{1}{2}} - \beta s_2 (m(\mathbf{q}))^{-\frac{3}{2}} \right) \frac{\partial^2 m(\mathbf{q})}{\partial q_{kr}^2} \\ & + \frac{1}{2} \left(-\frac{1}{2} s_1 (m(\mathbf{q}))^{-\frac{3}{2}} + \frac{3}{2} \beta s_2 (m(\mathbf{q}))^{-\frac{5}{2}} \right) \left(\frac{\partial m(\mathbf{q})}{\partial q_{kr}} \right)^2 \end{aligned} \quad (32)$$

with

$$\frac{\partial m(\mathbf{q})}{\partial q_{k1}} = 2g_{22}q_{k1} - 2g_{12}q_{k2}, \quad \frac{\partial m(\mathbf{q})}{\partial q_{k2}} = 2g_{11}q_{k2} - 2g_{12}q_{k1}, \quad (33)$$

$$\frac{\partial^2 m(\mathbf{q})}{\partial q_{k1}^2} = 2g_{22} - 2q_{k2}^2, \quad \frac{\partial^2 m(\mathbf{q})}{\partial q_{k2}^2} = 2g_{11} - 2q_{k1}^2 \quad (34)$$

for $k = 1, 2, 3$. From an initial guess of \mathbf{q}^0 , q_{kr} is updated by

$$q_{kr}^{\omega+1} = q_{kr}^{\omega} - \frac{\frac{\partial E_1}{\partial q_{kr}}(\mathbf{q}^{\omega}, \mathbf{p})}{\frac{\partial^2 E_1}{\partial q_{kr}^2}(\mathbf{q}^{\omega}, \mathbf{p})} \quad (35)$$

until $\max_{k,r} |q_{kr}^{\omega+1} - q_{kr}^{\omega}|_{\infty} < tol$ for some stopping criterion tol . Then we set $q_{kr}^{n+1/3} = q_{kr}^*$ where q_{kr}^* is the converged variable.

For $\boldsymbol{\lambda}^{n+1/3}$, it is the solution to

$$\begin{cases} \boldsymbol{\lambda}^{n+1/3} = \{\boldsymbol{\lambda}_k^{n+1/3}\}_{k=1}^3 \in (H^1(\Omega))^{3 \times 2}, \\ \gamma_1 \int_{\Omega} \boldsymbol{\lambda}_k^{n+1/3} \cdot \boldsymbol{\mu}_k dx + 2\beta\tau \int_{\Omega} \frac{(\nabla \cdot \boldsymbol{\lambda}_k^{n+1/3})(\nabla \cdot \boldsymbol{\mu}_k)}{\sqrt{g^{n+1/3}}} dx = \gamma_1 \int_{\Omega} \boldsymbol{\lambda}_k^n \cdot \boldsymbol{\mu}_k dx, \\ \forall \boldsymbol{\mu}_k \in (H(\Omega))^2, k = 1, 2, 3, \end{cases} \quad (36)$$

which is equivalent to

$$\begin{cases} \gamma_1 \boldsymbol{\lambda}_k^{n+1/3} - 2\beta\tau \nabla \left(\frac{\nabla \cdot \boldsymbol{\lambda}_k^{n+1/3}}{\sqrt{g^{n+1/3}}} \right) = \gamma_1 \boldsymbol{\lambda}_k^n \text{ in } \Omega, \\ \nabla \cdot \boldsymbol{\lambda}_k^{n+1/3} = 0 \text{ on } \partial\Omega, \\ k = 1, 2, 3. \end{cases} \quad (37)$$

Problem (37) (and (47) in Section 4.5) is a simple linear PDE. In the case that Ω is a rectangle, there are many fast solvers (like sparse Cholesky, conjugate gradient and cyclic reduction to name a few) for this kind of problems. In this paper, the periodic boundary condition is assumed for all variables. After enforcing the periodic boundary condition, we solve

$$\begin{cases} \gamma_1 \boldsymbol{\lambda}_k^{n+1/3} - 2\beta\tau \nabla \left(\frac{\nabla \cdot \boldsymbol{\lambda}_k^{n+1/3}}{\sqrt{g^{n+1/3}}} \right) = \gamma_1 \boldsymbol{\lambda}_k^n \text{ in } \Omega, \\ \boldsymbol{\lambda}_k^{n+1/3} \text{ has periodic boundary condition,} \\ k = 1, 2, 3. \end{cases} \quad (38)$$

4.4 On the solution of (27) and the choice of γ_1

The solution $(\mathbf{p}^{n+2/3}, \boldsymbol{\lambda}^{n+2/3})$ is the minimizer of

$$(\mathbf{p}^{n+2/3}, \boldsymbol{\lambda}^{n+2/3}) = \arg \min_{(\mathbf{q}, \boldsymbol{\mu}) \in S_{\mathbf{G}^{n+1/3}}} \int_{\Omega} \left(|\mathbf{q} - \mathbf{p}^{n+1/3}|^2 + \gamma_1 |\boldsymbol{\mu} - \boldsymbol{\lambda}^{n+1/3}|^2 \right) dx. \quad (39)$$

Recall that

$$S_{\mathbf{G}} = \{(\mathbf{q}, \boldsymbol{\mu}) \in ((L^2(\Omega))^{3 \times 2}, (L^2(\Omega))^{3 \times 2}), \boldsymbol{\mu}_k = \sqrt{g} \mathbf{q}_k \mathbf{G}^{-1}, k = 1, 2, 3 \text{ with } g = \det \mathbf{G}\}.$$

Thus, we have $\mathbf{q} = \frac{1}{\sqrt{g^{n+1/3}}} \boldsymbol{\mu} \mathbf{G}^{n+1/3}$. Substituting this into (39), the right hand side becomes a functional of $\boldsymbol{\mu}$ only:

$$E_2 = \int_{\Omega} \left(\left| \frac{1}{\sqrt{g^{n+1/3}}} \boldsymbol{\mu} \mathbf{G}^{n+1/3} - \mathbf{p}^{n+1/3} \right|^2 + \gamma_1 |\boldsymbol{\mu} - \boldsymbol{\lambda}^{n+1/3}|^2 \right) dx. \quad (40)$$

For simplicity, we temporally use $g, g_{kr}, p_{kr}, \lambda_{kr}$ to denote $g^{n+1/3}, g_{kr}^{n+1/3}, p_{kr}^{n+1/3}, \lambda_{kr}^{n+1/3}$ in this subsection. Computing the variation of E_2 with respect to $\boldsymbol{\mu}_k$ gives

$$\frac{\partial E_2}{\partial \boldsymbol{\mu}_k} = \begin{pmatrix} A_{11} & A_{12} \\ A_{21} & A_{22} \end{pmatrix} \begin{pmatrix} \mu_{k1} \\ \mu_{k2} \end{pmatrix} - \begin{pmatrix} b_1 \\ b_2 \end{pmatrix} \quad (41)$$

with

$$A_{11} = \frac{2g_{11}^2 + 2g_{12}^2}{g} + 2\gamma_1, \quad A_{12} = A_{21} = \frac{2g_{11}g_{12} + 2g_{12}g_{22}}{g}, \quad A_{22} = \frac{2g_{12}^2 + 2g_{22}^2}{g} + 2\gamma_1$$

$$b_1 = \frac{2g_{11}p_{k1} + 2g_{21}p_{k2}}{\sqrt{g}} + 2\gamma_1\lambda_{k1}, \quad b_2 = \frac{2g_{12}p_{k1} + 2g_{22}p_{k2}}{\sqrt{g}} + 2\gamma_1\lambda_{k2}.$$

By the optimality condition, we get that

$$\begin{pmatrix} \lambda_{k1}^{n+2/3} \\ \lambda_{k2}^{n+2/3} \end{pmatrix} = \frac{1}{A_{11}A_{22} - A_{12}A_{21}} \begin{pmatrix} A_{22}b_1 - A_{12}b_2 \\ -A_{21}b_1 + A_{11}b_2 \end{pmatrix} \quad (42)$$

for $k = 1, 2, 3$. And $\mathbf{p}_k^{n+1/3}$ is computed as

$$\mathbf{p}_k^{n+2/3} = \frac{1}{\sqrt{g^{n+1/3}}} \boldsymbol{\lambda}_k^{n+2/3} \mathbf{G}^{n+1/3}. \quad (43)$$

For the choice of γ_1 , we want to chose γ_1 such that the two terms in (39) are balanced. Since $\boldsymbol{\mu} = \sqrt{g}\mathbf{p}\mathbf{G}^{-1}$, we have

$$\frac{\partial \boldsymbol{\mu}}{\partial t} = \sqrt{g} \frac{\partial \mathbf{p}}{\partial t} \mathbf{G}^{-1}. \quad (44)$$

The integrand in (39) can be approximated as

$$\left| \mathbf{p}^{n+2/3} - \mathbf{p}^{n+1/3} \right|^2 + \gamma_1 \left| \boldsymbol{\lambda}^{n+2/3} - \boldsymbol{\lambda}^{n+1/3} \right|^2 \approx \tau^2 \left(\left| \frac{\partial \mathbf{p}}{\partial t}(t^{n+1/3}) \right|^2 + \gamma_1 \left| \frac{\partial \boldsymbol{\mu}}{\partial t}(t^{n+1/3}) \right|^2 \right). \quad (45)$$

Denote the eigenvalues of \mathbf{G} by ρ_1, ρ_2 . To balance the two terms, the above estimations suggest using $\gamma_1 = \sqrt{g}/\min\{\rho_1, \rho_2\}$. Since $g = \det \mathbf{G} = \rho_1\rho_2$, we approximate $\min\{\rho_1, \rho_2\} \approx \sqrt{g}$ which gives rise to $\gamma_1 = 1$.

4.5 On the solution of (28)

In (28), since $v_{\mathbf{q},g}$ is the solution to (14), we write \mathbf{p}^{n+1} as $\nabla \mathbf{u}^{n+1}$ for $\mathbf{u}^{n+1} = (u_1^{n+1}, u_2^{n+1}, u_3^{n+1})^T$. If \mathbf{p}^{n+1} minimizes (28), \mathbf{u}^{n+1} is the solution to

$$\begin{cases} u^{n+1} \in (H^1(\Omega))^3, \\ \sum_{k=1}^3 \left(\eta \int_{\Omega} \nabla u_k^{n+1} \cdot \nabla v_k dx + \tau \int_{\Omega} u_k^{n+1} v_k dx \right) = \\ \quad \sum_{k=1}^3 \left(\eta \int_{\Omega} \mathbf{p}_k^{n+2/3} \cdot \nabla v_k dx + \tau \int_{\Omega} f_k v_k dx \right), \\ \forall v \in (H^1(\Omega))^3, \\ \int_{\Omega} u_k^{n+1} dx = \int_{\Omega} f_k dx, \quad k = 1, 2, 3. \end{cases} \quad (46)$$

Equivalently, \mathbf{u}^{n+1} is the weak solution of

$$\begin{cases} -\eta \nabla^2 u_k^{n+1} + \tau u_k^{n+1} = -\eta \nabla \cdot \mathbf{p}_k^{n+2/3} + \tau f_k \text{ in } \Omega, \\ (\nabla u_k^{n+1} - \mathbf{p}_k^{n+2/3}) \cdot \mathbf{n} = 0 \text{ on } \partial\Omega, \\ k = 1, 2, 3. \end{cases} \quad (47)$$

After enforcing the periodic boundary condition, we solve

$$\begin{cases} -\eta \nabla^2 u_k^{n+1} + \tau u_k^{n+1} = -\eta \nabla \cdot \mathbf{p}_k^{n+2/3} + \tau f_k \text{ in } \Omega, \\ u_k^{n+1} \text{ has periodic boundary condition,} \\ k = 1, 2, 3. \end{cases} \quad (48)$$

Problem (48) can be solved by FFT. Once it has been solved, \mathbf{p}^{n+1} is updated as $\mathbf{p}^{n+1} = \nabla \mathbf{u}^{n+1}$.

5 Space discretization

5.1 Basic discrete operators

We assume $\Omega \in \mathbb{R}^2$ to be a rectangle with $M \times N$ pixels. x_1, x_2 are used to denote the two spatial directions along which all functions are assumed to be periodic. We use spacial step $\Delta x_1 = \Delta x_2 = h$. For a vector-valued function $\mathbf{f} = (f_1, f_2, f_3)^T$ (resp. scalar-valued function f) defined on Ω , we denote its (i, j) -th pixel by $\mathbf{f}(i, j) = (f_1(i, j), f_2(i, j), f_3(i, j))^T$ (resp. $f(i, j)$). By taking into account the periodic boundary condition, the backward $(-)$ and forward $(+)$ approximation for $\partial f / \partial x_1$ and $\partial f / \partial x_2$ are defined as

$$\begin{aligned}\partial_1^- f(i, j) &= \begin{cases} \frac{f(i, j) - f(i-1, j)}{h}, & 1 < i \leq M, \\ \frac{f(1, j) - f(M, j)}{h}, & i = 1, \end{cases} & \partial_1^+ f(i, j) &= \begin{cases} \frac{f(i+1, j) - f(i, j)}{h}, & 1 \leq i < M, \\ \frac{f(1, j) - f(M, j)}{h}, & i = M, \end{cases} \\ \partial_2^- f(i, j) &= \begin{cases} \frac{f(i, j) - f(i, j-1)}{h}, & 1 < i \leq N, \\ \frac{f(i, 1) - f(i, N)}{h}, & i = 1, \end{cases} & \partial_2^+ f(i, j) &= \begin{cases} \frac{f(i, j+1) - f(i, j)}{h}, & 1 \leq i < N, \\ \frac{f(i, 1) - f(i, N)}{h}, & i = N. \end{cases}\end{aligned}$$

Based on the above notations, the backward $(-)$ and forward $(+)$ approximation of the gradient ∇ and the divergence div are defined as

$$\nabla^\pm f(i, j) = (\partial_1^\pm f(i, j), \partial_2^\pm f(i, j)), \quad \text{div}^\pm \mathbf{p}(i, j) = \partial_1^\pm p_1(i, j) + \partial_2^\pm p_2(i, j).$$

We denote the discrete Fourier transform and its inverse by \mathcal{F} and \mathcal{F}^{-1} , respectively. It is obvious that

$$\mathcal{F}(f)(i \pm 1, j) = e^{\pm 2\pi\sqrt{-1}(i-1)/M} \mathcal{F}(f)(i, j), \quad \mathcal{F}(f)(i, j \pm 1) = e^{\pm 2\pi\sqrt{-1}(j-1)/N} \mathcal{F}(f)(i, j).$$

We use $\text{Real}(\cdot)$ to denote the real part of its argument. The shifting and identity operator are defined as

$$\mathcal{S}_1^\pm f(i, j) = f(i \pm 1, j), \quad \mathcal{S}_2^\pm f(i, j) = f(i, j \pm 1), \quad \mathcal{I}f(i, j) = f(i, j). \quad (49)$$

5.2 Numerical solution for $\mathbf{p}^{n+1/3}$ in (29)

In this subsection we discretize the updating formula of $\mathbf{p}^{n+1/3}$ in problem (29). We set $s_1 = 1$. In s_2 , the divergence is approximated by $\nabla \cdot \boldsymbol{\lambda}_k^n = \text{div}^- \boldsymbol{\lambda}_k^n$ for $k = 1, 2, 3$. s_2 is computed as

$$s_2(i, j) = \sum_{k=1}^3 |\text{div}^- \boldsymbol{\lambda}_k^n(i, j)|^2.$$

Then $\partial E_1 / \partial q_{kr}$, $\partial^2 E_1 / \partial q_{kr}^2$, $\partial m / \partial q_{kr}$ and $\partial^2 m / \partial q_{kr}^2$ can be computed pointwisely. Set an initial condition $\mathbf{q}^{(0)}$, \mathbf{q} is updated through (35) until converge. Denoting the converged variable by \mathbf{q}^* , we update $\mathbf{p}^{n+1/3} = \mathbf{q}^*$. In our algorithm, $\mathbf{q}^{(0)} = \mathbf{q}^n$ is used.

5.3 Numerical solution for $\boldsymbol{\lambda}^{n+1/3}$ in (38)

Problem (38) is discretized as

$$\gamma_1 \boldsymbol{\lambda}_k^{n+1/3} - 2\beta\tau \nabla^+ \left(\frac{\text{div}^- \boldsymbol{\lambda}_k^{n+1/3}}{\sqrt{g^{n+1/3}}} \right) = \gamma_1 \boldsymbol{\lambda}_k^n \quad (50)$$

for $k = 1, 2, 3$. Instead of solving (50), we use the *frozen coefficient approach* (see [8, 16]) to solve

$$\gamma_1 \boldsymbol{\lambda}_k^{n+1/3} - c_1 \nabla^+ (\text{div}^- \boldsymbol{\lambda}_k^{n+1/3}) = \gamma_1 \boldsymbol{\lambda}_k^n - \nabla^+ \left[\left(c_1 - 2\beta\tau / \sqrt{g^{n+1/3}} \right) \text{div}^- \boldsymbol{\lambda}_k^n \right] \quad (51)$$

with some properly chosen c_1 . We suggest to use $c_1 = \max_{i,j} 2\beta\tau/\sqrt{g^{n+1/3}(i,j)}$. (51) can be written in matrix form

$$\begin{pmatrix} \gamma_1 - c_1 \partial_1^+ \partial_1^- & -c_1 \partial_1^+ \partial_2^- \\ -c_1 \partial_2^+ \partial_1^- & \gamma_1 - c_1 \partial_2^+ \partial_2^- \end{pmatrix} \begin{pmatrix} \lambda_{k1}^{n+1/3} \\ \lambda_{k2}^{n+1/3} \end{pmatrix} = \begin{pmatrix} w_1 \\ w_2 \end{pmatrix} \quad (52)$$

with

$$\begin{aligned} w_1 &= \gamma_1 \lambda_{k1}^n - \partial_1^+ \left[\left(c_1 - 2\beta\tau/\sqrt{g^{n+1/3}} \right) \operatorname{div}^- \boldsymbol{\lambda}_k^n \right], \\ w_2 &= \gamma_1 \lambda_{k2}^n - \partial_2^+ \left[\left(c_1 - 2\beta\tau/\sqrt{g^{n+1/3}} \right) \operatorname{div}^- \boldsymbol{\lambda}_k^n \right]. \end{aligned}$$

The linear system (52) is equivalent to

$$\begin{pmatrix} \gamma_1 - c_1(\mathcal{S}_1^+ - \mathcal{I})(\mathcal{I} - \mathcal{S}_1^-)/h^2 & -c_1(\mathcal{S}_1^+ - \mathcal{I})(\mathcal{I} - \mathcal{S}_2^-)/h^2 \\ -c_1(\mathcal{S}_2^+ - \mathcal{I})(\mathcal{I} - \mathcal{S}_1^-)/h^2 & \gamma_1 - c_1(\mathcal{S}_2^+ - \mathcal{I})(\mathcal{I} - \mathcal{S}_2^-)/h^2 \end{pmatrix} \begin{pmatrix} \lambda_{k1}^{n+1/3} \\ \lambda_{k2}^{n+1/3} \end{pmatrix} = \begin{pmatrix} w_1 \\ w_2 \end{pmatrix}. \quad (53)$$

Applying the discrete Fourier transform on both sides gives rise to

$$\begin{pmatrix} a_{11} & a_{12} \\ a_{21} & a_{22} \end{pmatrix} \mathcal{F} \begin{pmatrix} \lambda_{k1}^{n+1/3} \\ \lambda_{k2}^{n+1/3} \end{pmatrix} = \mathcal{F} \begin{pmatrix} w_1 \\ w_2 \end{pmatrix}$$

where

$$\begin{aligned} a_{11} &= \gamma_1 - 2c_1(\cos z_i - 1)/h^2, \quad a_{22} = \gamma_1 - 2c_1(\cos z_j - 1)/h^2, \\ a_{12} &= -c_1(1 - \cos z_i - \sqrt{-1} \sin z_i)(1 - \cos z_j + \sqrt{-1} \sin z_j)/h^2, \\ a_{21} &= -c_1(1 - \cos z_j - \sqrt{-1} \sin z_j)(1 - \cos z_i + \sqrt{-1} \sin z_i)/h^2, \end{aligned}$$

with $z_i = 2\pi(i-1)/M$, $z_j = 2\pi(j-1)/N$ for $i = 1, \dots, M$ and $j = 1, \dots, N$. We have

$$\begin{pmatrix} \lambda_{k1}^{n+1/3} \\ \lambda_{k2}^{n+1/3} \end{pmatrix} = \operatorname{Real} \left(\mathcal{F}^{-1} \left[\frac{1}{a_{11}a_{22} - a_{12}a_{21}} \begin{pmatrix} a_{22}\mathcal{F}(w_1) - a_{12}\mathcal{F}(w_2) \\ -a_{21}\mathcal{F}(w_1) + a_{11}\mathcal{F}(w_2) \end{pmatrix} \right] \right).$$

5.4 Numerical solution for $(\mathbf{p}^{n+2/3}, \boldsymbol{\lambda}^{n+2/3})$ in (39)

(39) can be written as the energy E_2 (in (40)) which is a quadratic functional of μ . $\boldsymbol{\lambda}^{n+2/3}$ can be updated by solving (42) pointwisely. Then we update

$$\mathbf{p}_k^{n+2/3} = \frac{1}{\sqrt{g^{n+1/3}}} \boldsymbol{\lambda}_k^{n+2/3} \mathbf{G}^{n+1/3}. \quad (54)$$

for $k = 1, 2, 3$.

5.5 Numerical solution for \mathbf{p}^{n+1} in (48)

We update \mathbf{p}^{n+1} as $\nabla \mathbf{u}^{n+1}$ where $\mathbf{u}^{n+1} = (u_1^{n+1}, u_2^{n+1}, u_3^{n+1})^T$ is the solution of

$$\begin{cases} -\eta \nabla^2 u_k^{n+1} + \tau u_k^{n+1} = -\eta \nabla \cdot \mathbf{p}_k^{n+2/3} + \tau f_k, \\ u_k^{n+1} \text{ has periodic boundary condition.} \end{cases} \quad (55)$$

We discrete (55) as

$$-\eta \operatorname{div}^-(\nabla^+ u_k^{n+1}) + \tau u_k^{n+1} = -\eta \operatorname{div}^- \mathbf{p}_k^{n+2/3} + \tau f_k \quad (56)$$

| | Portrait | | Chips | |
|--------------------|-------------|-------------|-------------|-------------|
| | $SD = 0.03$ | $SD = 0.06$ | $SD = 0.03$ | $SD = 0.06$ |
| The proposed model | 36.66 | 33.09 | 37.19 | 33.89 |
| Method from [18] | 32.97 | 29.55 | 34.00 | 30.76 |

Table 1: With Gaussian noise, comparison of the PSNR values of the proposed method and the method in [18].

which is equivalent to

$$[-\eta(\mathcal{I} - \mathcal{S}_1^-)(\mathcal{S}_1^+ - \mathcal{I})/h^2 - \eta(\mathcal{I} - \mathcal{S}_2^-)(\mathcal{S}_2^+ - \mathcal{I})/h^2 + c_1\mathcal{I}] u_k^{n+1} = b \quad (57)$$

with $b = -\eta \operatorname{div}^- \mathbf{p}_k^{n+2/3} + \tau f_k$. (57) can be solved efficiently by FFT,

$$u_k^{n+1} = \operatorname{Real} \left[\mathcal{F}^{-1} \left(\frac{\mathcal{F}(b)}{w} \right) \right] \quad (58)$$

where

$$w(i, j) = \tau \mathcal{I} - \eta \left(1 - e^{-\sqrt{-1}z_i} \right) \left(e^{\sqrt{-1}z_i} - 1 \right) / h^2 - \eta \left(1 - e^{-\sqrt{-1}z_j} \right) \left(e^{\sqrt{-1}z_j} - 1 \right) / h^2 \quad (59)$$

with z_i, z_j defined in Section 5.3. Then we update

$$\mathbf{p}_k^{n+1} = \nabla^+ u_k^{n+1}. \quad (60)$$

5.6 Initialization

For initial condition, we initialize $\mathbf{u}^0, \mathbf{p}^0 = (\mathbf{p}_1^0, \mathbf{p}_2^0, \mathbf{p}_3^0)^T$ as

$$\mathbf{u}^0 = \mathbf{f} \text{ and } \mathbf{p}_k^0 = \nabla^+ u_k^0 \quad (61)$$

for $k = 1, 2, 3$. Then we initialize

$$\mathbf{G}^0 = \mathbf{M}(\mathbf{p}^0), g^0 = m(\mathbf{G}^0). \quad (62)$$

$\boldsymbol{\lambda}^0 = (\boldsymbol{\lambda}_1^0, \boldsymbol{\lambda}_2^0, \boldsymbol{\lambda}_3^0)^T$ is computed as

$$\boldsymbol{\lambda}_k^0 = \sqrt{g^0} \mathbf{p}^0 \mathbf{G}^{-1} = \frac{1}{\sqrt{g^0}} \begin{pmatrix} g_{22}^0 p_{k1}^0 - g_{12}^0 p_{k2}^0 \\ -g_{21}^0 p_{k1}^0 + g_{11}^0 p_{k2}^0 \end{pmatrix}. \quad (63)$$

6 Numerical experiments

In this section, we present numerical results that demonstrate the effectiveness of the proposed model and solver. For all of the images used, the pixel values are in $[0, 1]$. For simplicity, $h = 1$ is used. For all experiments, $tol = 10^{-6}$ for is used in the Newton method (35) to update $\mathbf{p}^{n+1/3}$.

We consider noisy images with Gaussian noise and Poisson noise. For the Gaussian noise, the parameter is the standard deviation (denoted by SD). The larger SD is, the heavier the noise. In the Poisson noise case, the parameter is the number of photons (denoted by P). Images have better quality with more photons. When adding the Poisson noise, we use the MATLAB function *imnoise*. To add Poisson noise with P photons to an image \mathbf{v} , we refer to the function as *imnoise*($\mathbf{v} * P/10^{12}$, 'poisson')*10¹²/P.

In our experiments, when not specified otherwise, we use $\tau = 0.05, \gamma_1 = 1, \gamma_2 = 3, c_1 = \max_{i,j} 2\beta\tau/\sqrt{g^{n+1/3}(i,j)}$, and stopping criterion $\|u^{n+1} - u^n\|_2 \leq 10^{-2}$.

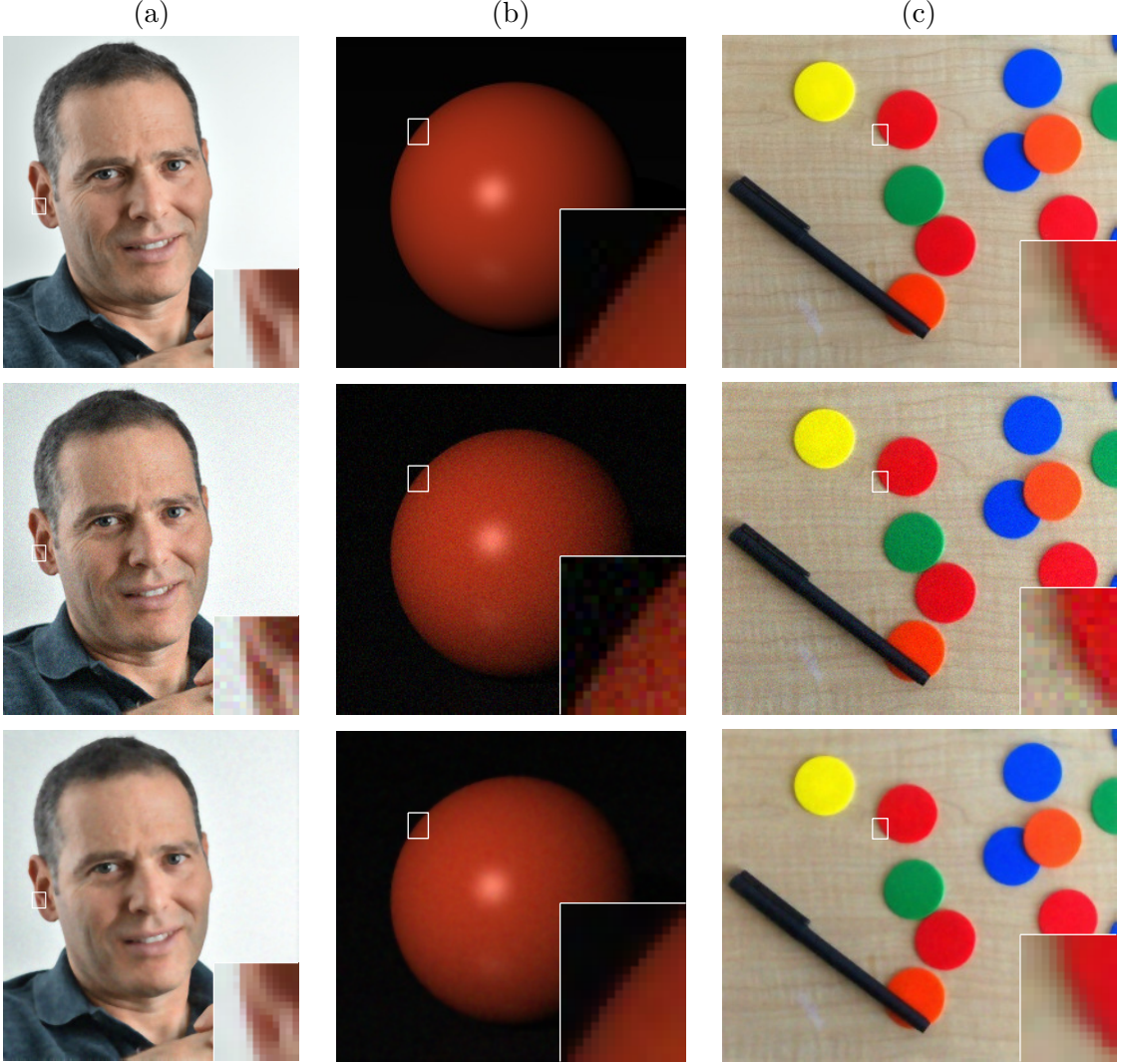


Figure 1: (Gaussian noise with $SD = 0.03$. $\alpha = 0.01, \eta = 0.5$.) Image denoising by the proposed method on (a) the portrait, (b) the orange ball and (c) chips. The first row shows clean images. The second row shows noisy images. The third row shows denoised images. $\beta = 0.01$ is used for the orange ball, and $\beta = 0.005$ is used for the portrait and chips.

6.1 Image denoising for the Gaussian noise

We use the proposed model to denoise images with Gaussian noise. We add Gaussian noise with $SD = 0.03$ to three images: (a) portrait, (b) orange ball and (c) chips (shown in the first row of Figure 1). The noisy images and denoised images with $\alpha = 0.01, \eta = 0.5$ are shown in the second and third rows of Figure 1, respectively. $\beta = 0.01$ is used for the orange ball, and $\beta = 0.005$ is used for the portrait and chips. For all of three examples, while they are denoised, sharp edges are kept. To demonstrate the efficiency of the proposed method, in Figure 2, we present the evolution of the energy and $\|u^{n+1} - u^n\|_2$ of the three examples shown in Figure 1. For the three examples, the energy decreases very fast and achieves the minimum within 40 iterations. Linear convergence is observed on the evolution of $\|u^{n+1} - u^n\|_2$.

We next add heavy Gaussian noise with $SD = 0.06$ to these images. The noisy and denoised images are shown in Figure 3. The evolution of the energy w.r.t. the number of iterations are also shown in the third row. Our method is efficient and performs well. The energy achieves its minimum within 70 iterations. In Table 1, we show the comparison of the PSNR value of the results by the proposed method and by the method from [18] which minimizes the Polyakov

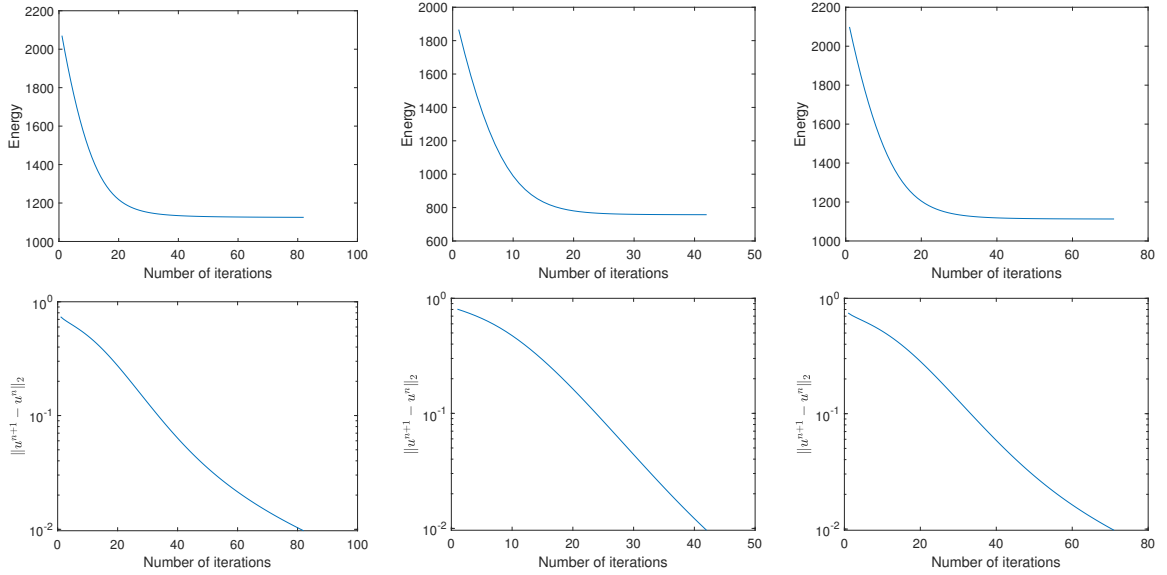


Figure 2: (Gaussian noise with $SD = 0.03$. $\alpha = 0.01$, $\eta = 0.5$.) The evolution of (first row) the energy and (second row) $\|u^{n+1} - u^n\|_2$ w.r.t. the number of iterations for results in Figure 1. First column: the portrait. Second column: the orange ball. Third column: chips. $\beta = 0.01$ is used for the orange ball, and $\beta = 0.005$ is used for the portrait and chips.

| | Lighthouse | | Stop sign | |
|--------------------|------------|-----------|-----------|-----------|
| | $P = 500$ | $P = 100$ | $P = 500$ | $P = 100$ |
| The proposed model | 35.55 | 30.67 | 36.33 | 32.05 |
| Method from [18] | 30.88 | 27.18 | 31.87 | 27.65 |

Table 2: With Poisson noise, comparison of the PSNR values of the proposed method and the method in [18].

action only. Our model has 3dB higher in the PSNR value. To better demonstrate the smoothing effect, we select the zoomed region of the orange ball and show the surface plot of each channel (RGB channel correspond the red, green and blue surface) in Figure 4. The surface plot of the noisy image is shown in the first row, which is very oscillating. The surface plot of the denoised image is shown in the second row. The surfaces of all three channels are very smooth which verifies the smoothing property of the proposed model. To further demonstrate the effectiveness of the proposed model, results on denoising Gaussian noise with $SD = 0.1$ are shown in Figure 5.

6.2 Image denoising for the Poisson noise

We explore the performance of the proposed method to denoise the Poisson noise with $P = 500$. Our examples are (a) the lighthouse, (b) stop sign and (c) vegetables, see the first row in Figure 6. The noisy images and denoised images with $\alpha = 0.01$, $\eta = 0.3$, $\beta = 0.005$ are shown as the second row and third row in Figure 6, respectively. Similar to the performance on the Gaussian noise, our method keeps sharp edges. The evolution of the energy and $\|u^{n+1} - u^n\|_2$ of these examples are shown in Figure 7. All energies achieve their minimum within 50 iteration.

Then, we add heavy Poisson noise with $P = 100$. The noisy and denoised images are shown in Figure 8. In this set of experiments, $\alpha = 0.01$, $\eta = 1$, $\beta = 0.005$ is used. We also show the evolution of energy against the number of iterations in Figure 9. All energies achieve their minimum in about 100 iterations. Figure 10 shows the surface plot of the zoomed region of the stop sign in Figure 8. The surface plot of the denoised image is smooth while that of the noisy

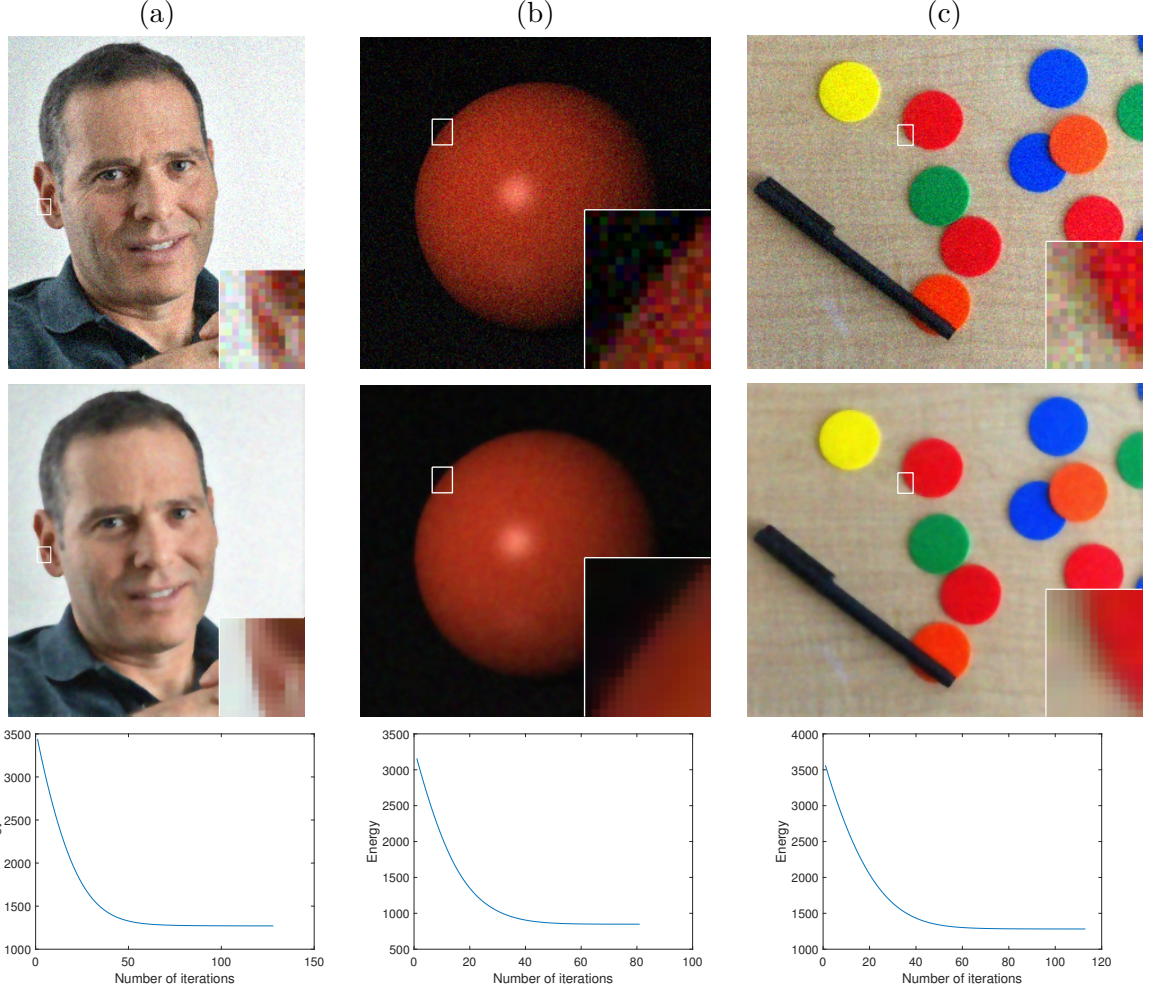


Figure 3: (Gaussian noise with $SD = 0.06$. $\alpha = 0.01, \eta = 1.$) Image denoising by the proposed method on (a) the portrait, (b) the orange ball and (c) chips. The first row shows noisy images. The second row shows denoised images. The third row shows the evolution of the energy w.r.t. the number of iterations. $\beta = 0.01$ is used for the orange ball, and $\beta = 0.005$ is used for the portrait and chips.

image is very oscillating. The comparison of the PSNR values of the results by the proposed model and by method from [18] is shown in Table 2. Similar to the comparison on Gaussian noise, for Poisson noise, the PSNR values of results by our proposed model are 3dB higher.

6.3 Effect of α

The regularization term (first term) in (8) depends on two quantities: the surface area \sqrt{g} and the color elastica $\sum_{k=1}^3 |\Delta_g u_k|^2$. Both terms are closely related to α . In this section, we explore the effect of α by checking the behavior of both terms w.r.t. the noise level with $\alpha = 10^{-1}, 10^{-2}, 10^{-3}, 10^{-4}$ and 10^{-5} . The images used are shown in Figure 11: (a) orange ball, (b) crystal cube and (c) fruits.

The first experiment involves Gaussian noise for which the noise level is controlled by SD : images have better quality with smaller SD . In Figure 12, we show the behavior of both terms w.r.t. SD . The first row shows the surface area and the second row shows the color elastica. Both terms have larger values on images with heavier noise (larger SD) for most choices of α , which justifies the effectiveness of the proposed model (8). In Figure 12, as SD gets larger, the surface area increases faster with smaller α while the color elastica increases faster with larger

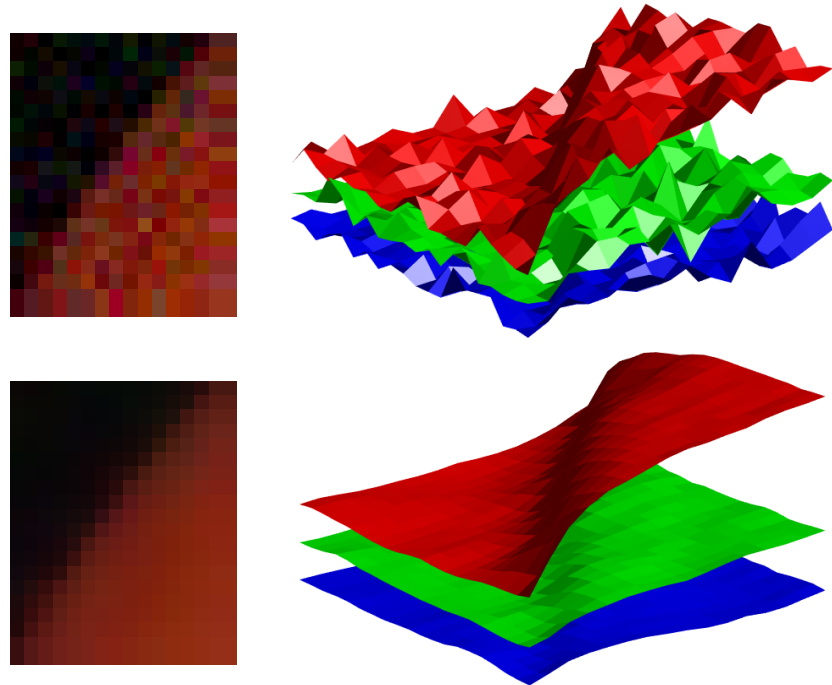


Figure 4: (Gaussian noise with $SD = 0.06$. Smoothing effect.) Left: zoomed region of the (first row) noisy and (second row) denoised orange ball in Figure 3. Right: the surface plot of the left images. The RGB channels corresponds to the red, green and blue surface, respectively.

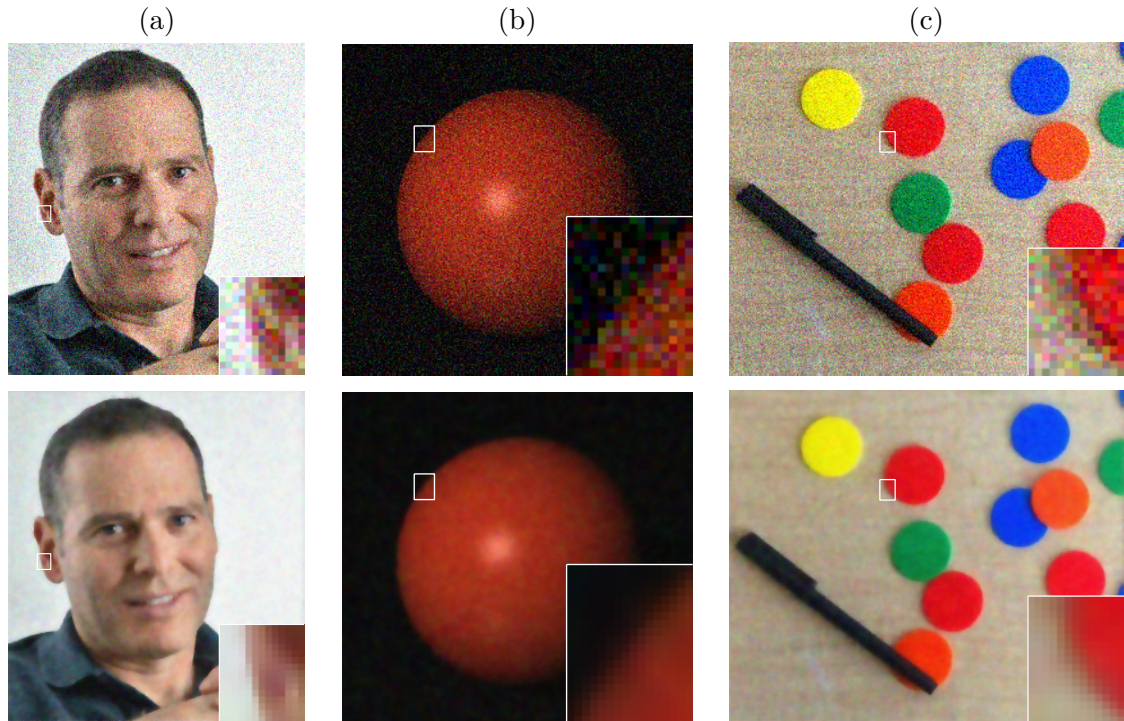


Figure 5: (Gaussian noise with $SD = 0.1$. $\alpha = 0.01, \eta = 2$.) Image denoising by the proposed method on (a) the portrait, (b) the orange ball and (c) chips. The first row shows noisy images. The second row shows denoised images. $\beta = 0.01$ is used for the orange ball, and $\beta = 0.005$ is used for the portrait and chips.

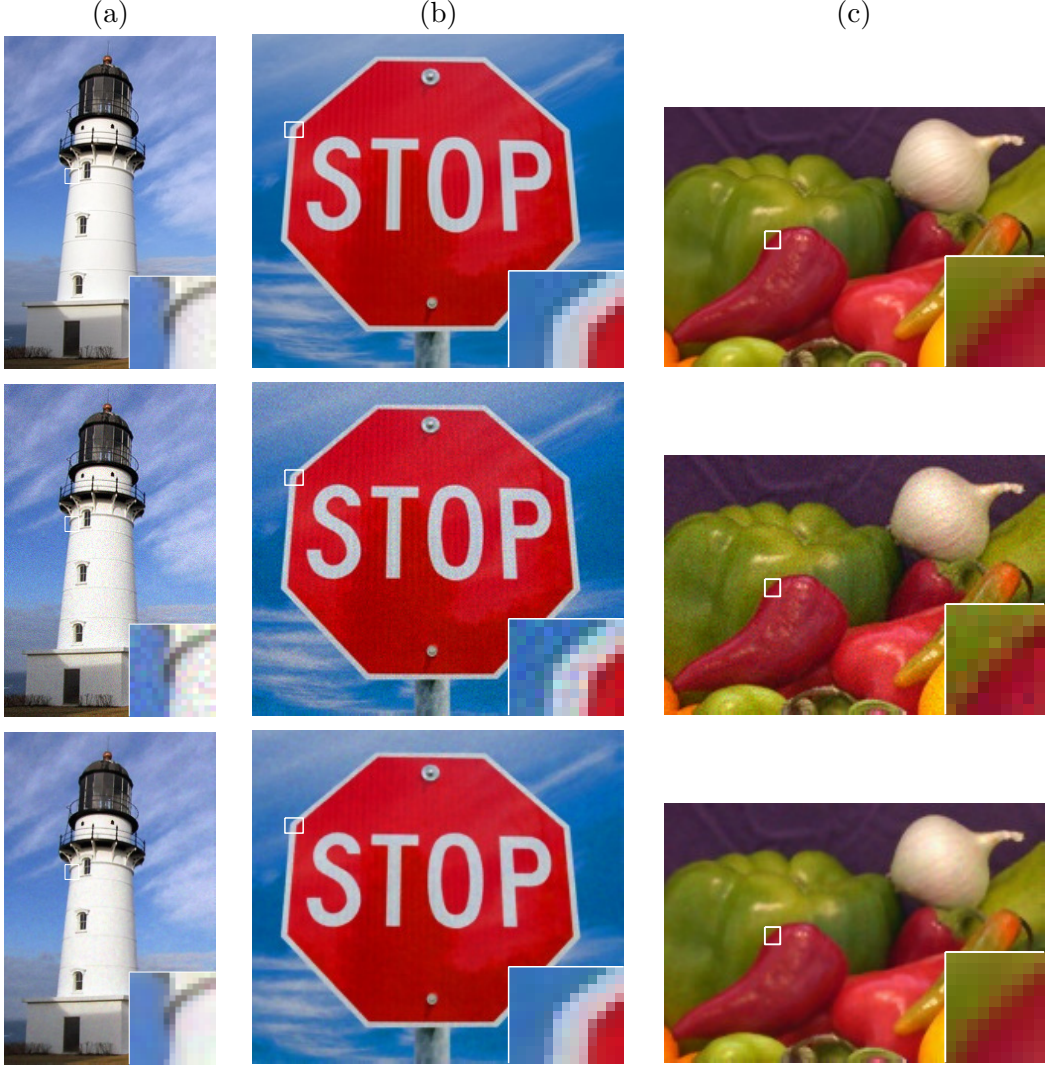


Figure 6: (Poisson noise with $P = 500$. $\alpha = 0.01$, $\eta = 0.3$, $\beta = 0.005$.) Image denoising by the proposed method on (a) the lighthouse, (b) the stop sign and (c) vegetables. The first row shows clean images. The second row shows noisy images. The third row shows denoised images.

α . To make both terms effective, α should not be too large or too small.

We then repeat these experiments on the Poisson noise in which the noise level is controlled by P , the number of photons. Images have better quality with larger P . The behavior of the surface area and energy w.r.t. P with different α is shown in Figure 13. Similar to the behavior for the Gaussian noise, both terms have larger values with heavier noise (smaller P). As α gets larger, the surface area has larger slope while the color elastica has smaller slope, which again implies that α should not be too large or too small to make both terms effective.

The above observation shows that the surface area is more effective with smaller α . However, even if our model only contains the surface area term (i.e., $\beta = 0$), we face the smoothness problem of edges if α is too small. In Figure 14, we use the proposed model with $\beta = 0$ and various α to denoise the orange ball which is contaminated by the Poisson noise with $P = 100$. The noisy image, denoised image with $\alpha = 10^{-1}, 10^{-2}, 10^{-3}, 10^{-4}$ and 10^{-5} are shown in (a)-(f), respectively. Since the scale of surface area changes as α , we need to set different η for each α . In our experiments, $\eta = 2, 2, 4, 8, 10$ are used as α varies from 10^{-1} to 10^{-5} . As α decreases, the edge of the orange ball in the denoised image becomes more oscillating. This may be a problem of the model itself or of our numerical algorithm which is to be studied in the future.

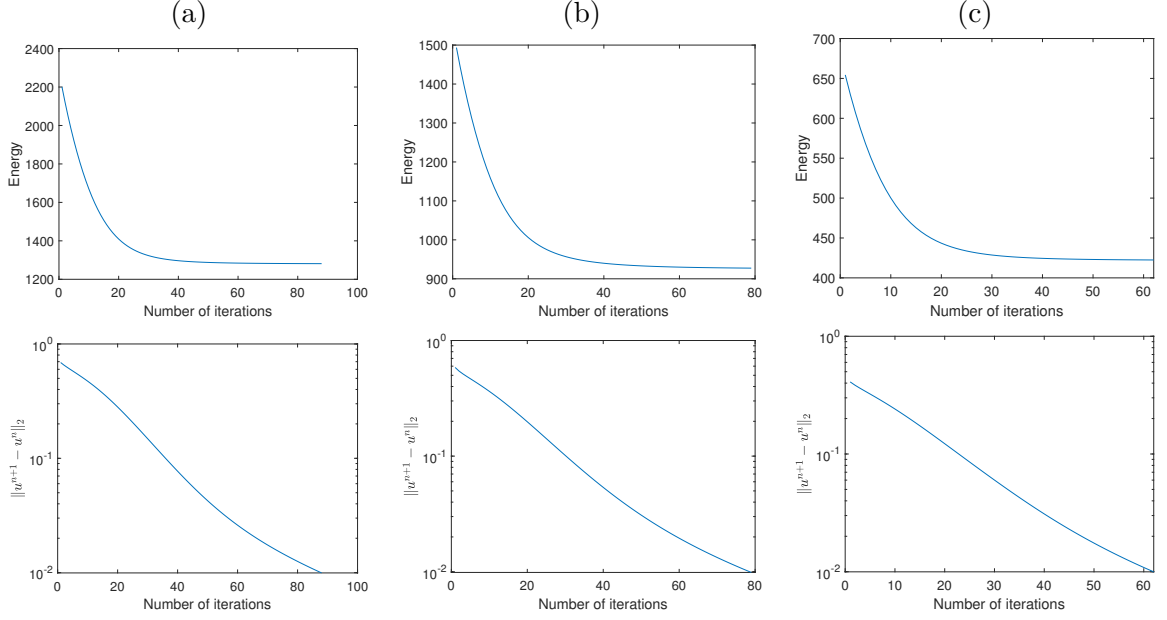


Figure 7: (Poisson noise with $P = 500$. $\alpha = 0.01, \eta = 0.3, \beta = 0.005$.) The evolution of (first row) the energy and (second row) $\|u^{n+1} - u^n\|_2$ w.r.t. the number of iterations for results in Figure 6. (a) the lighthouse. (b) the stop sign and (c) vegetables.

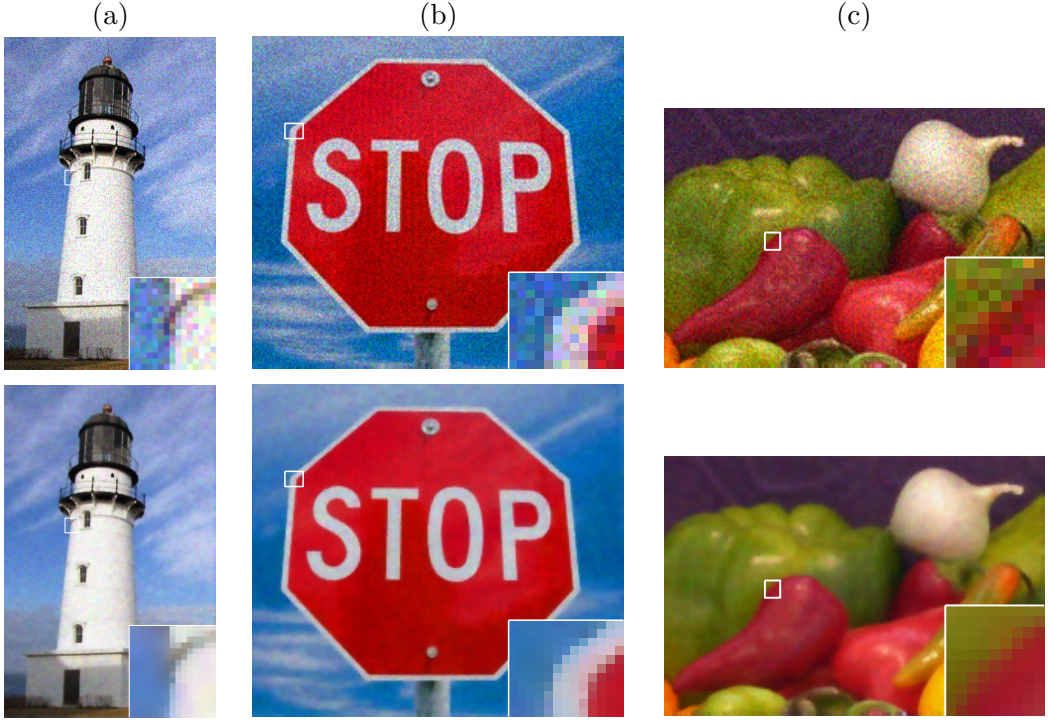


Figure 8: (Poisson noise with $P = 100$. $\alpha = 0.01, \eta = 1, \beta = 0.005$.) Image denoising by the proposed method on (a) the lighthouse, (b) the stop sign and (c) vegetables. The first row shows noisy images. The second row shows denoised images.

6.4 Effect of β

We fix $\alpha = 10^{-2}, \eta = 0.01$ and explore the effect of β on our model. We use the image of crystal cube (shown in Figure 15(a)) with the Gaussian noise with $SD = 0.06$. We test our model with

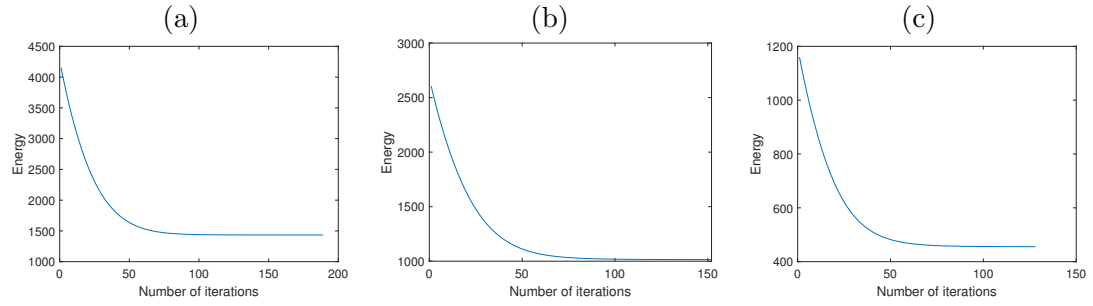


Figure 9: (Poisson noise with $P = 100$. $\alpha = 0.01, \eta = 1, \beta = 0.005$.) The evolution of the energy w.r.t. the number of iterations for results in Figure 8. (a) the lighthouse, (b) the stop sign and (c) vegetables.

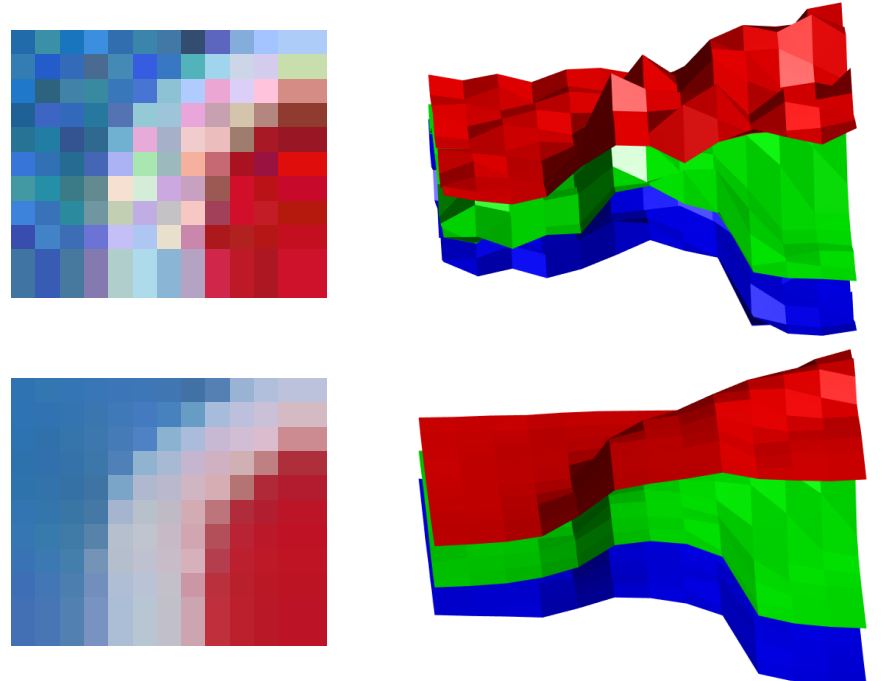


Figure 10: (Poisson noise with $P = 100$. Smoothing effect.) Left: zoomed region of the (first row) noisy and (second row) denoised stop sign in Figure 8. Right: the surface plot of the left images. The RGB channels correspond to the red, green and blue surface, respectively.

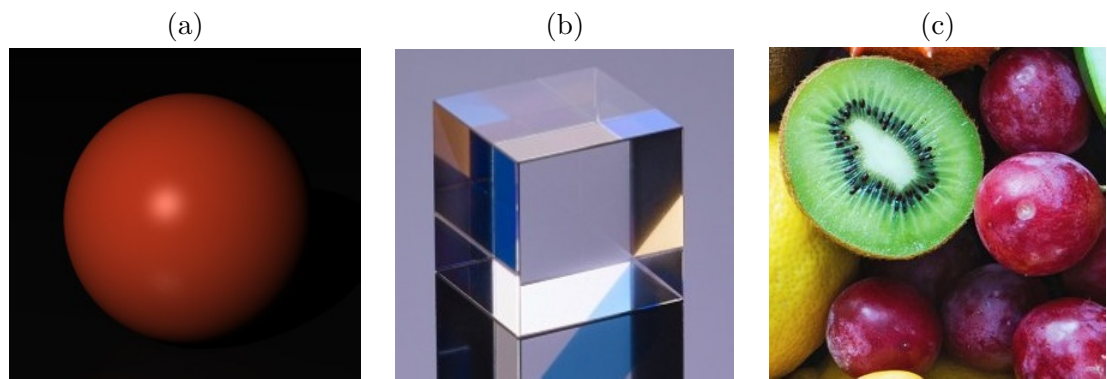


Figure 11: (Effect of α): (a) The orange ball. (b) The crystal cube. (c) Fruits.

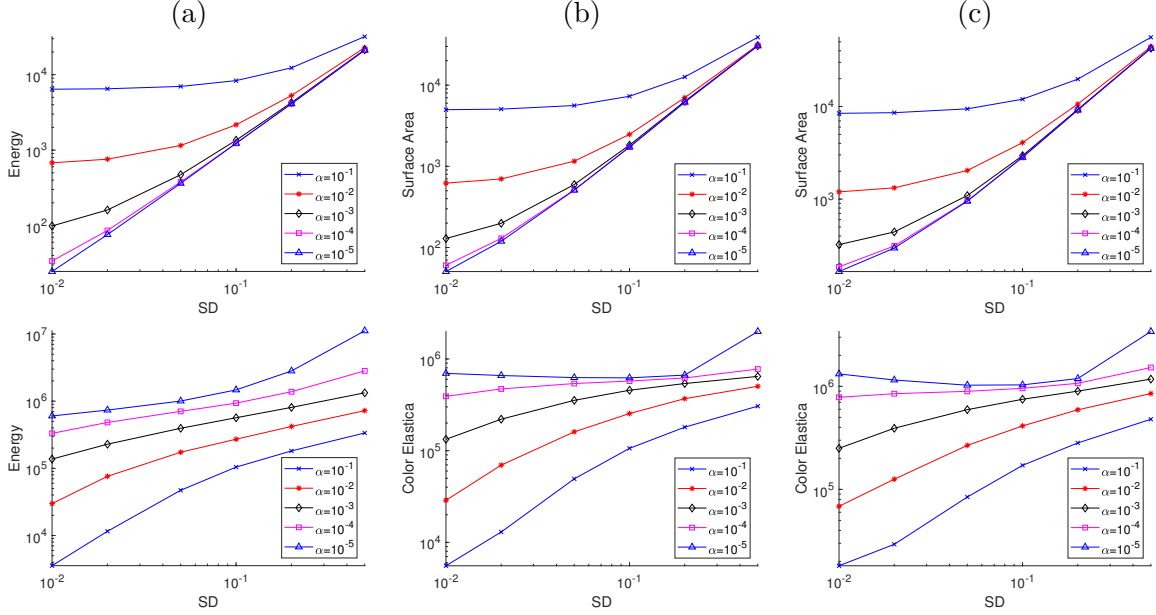


Figure 12: (Effect of α , Gaussian noise.) With $\alpha = 10^{-1}, 10^{-2}, 10^{-3}, 10^{-4}$ and 10^{-5} , plot of (first row) the surface area and (second row) the color elastica computed from noisy images w.r.t. SD . (a)-(c) corresponds to the orange ball, the crystal cube and fruits shown in Figure 11, respectively. Images have higher quality with smaller SD .

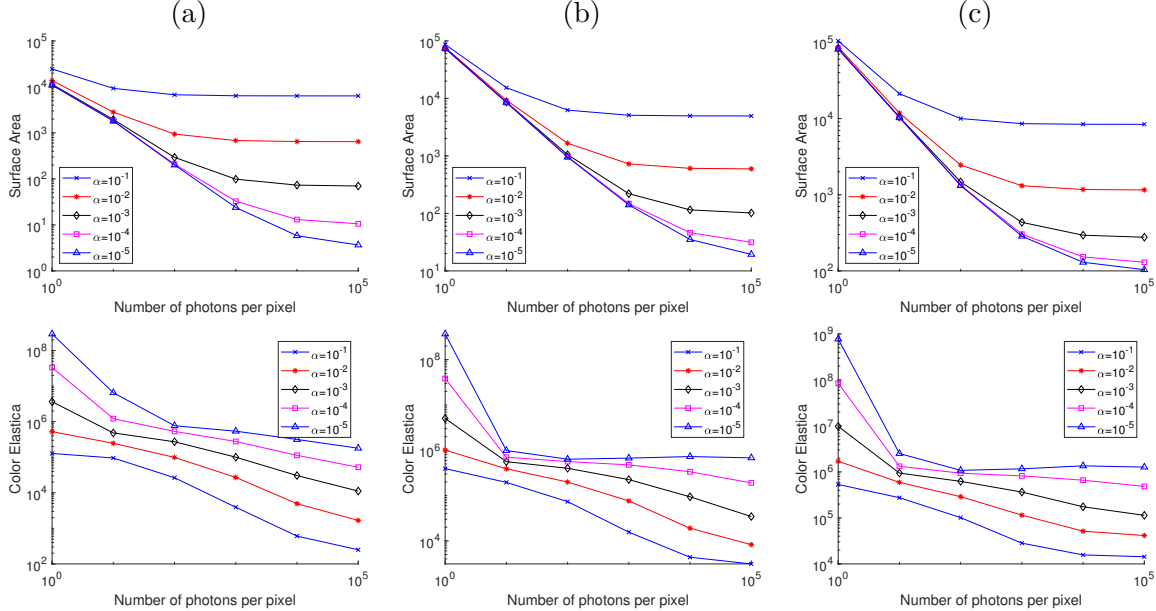


Figure 13: (Effect of α , Poisson noise.) With $\alpha = 10^{-1}, 10^{-2}, 10^{-3}, 10^{-4}$ and 10^{-5} , plot of (first row) the surface area and (second row) the color elastica computed from noisy images against P . (a)-(c) corresponds to the orange ball, the crystal cube and fruits shown in Figure 11, respectively. Images have higher quality with larger P .

$\beta = 0, 0.005, 0.1$ and 0.2 . The noisy and denoised images are shown in Figure 15. When $\beta = 0$, model (8) reduces to the Polyakov action model and there are perturbations in the flat region of the denoised image, see Figure 15(c). As β gets larger, the flat part of the denoised image becomes smoother while the edges are kept. Similar to the elastica model for greyscale images, the color elastica term helps smoothing the flat region. In Figure 16 we compare the surface

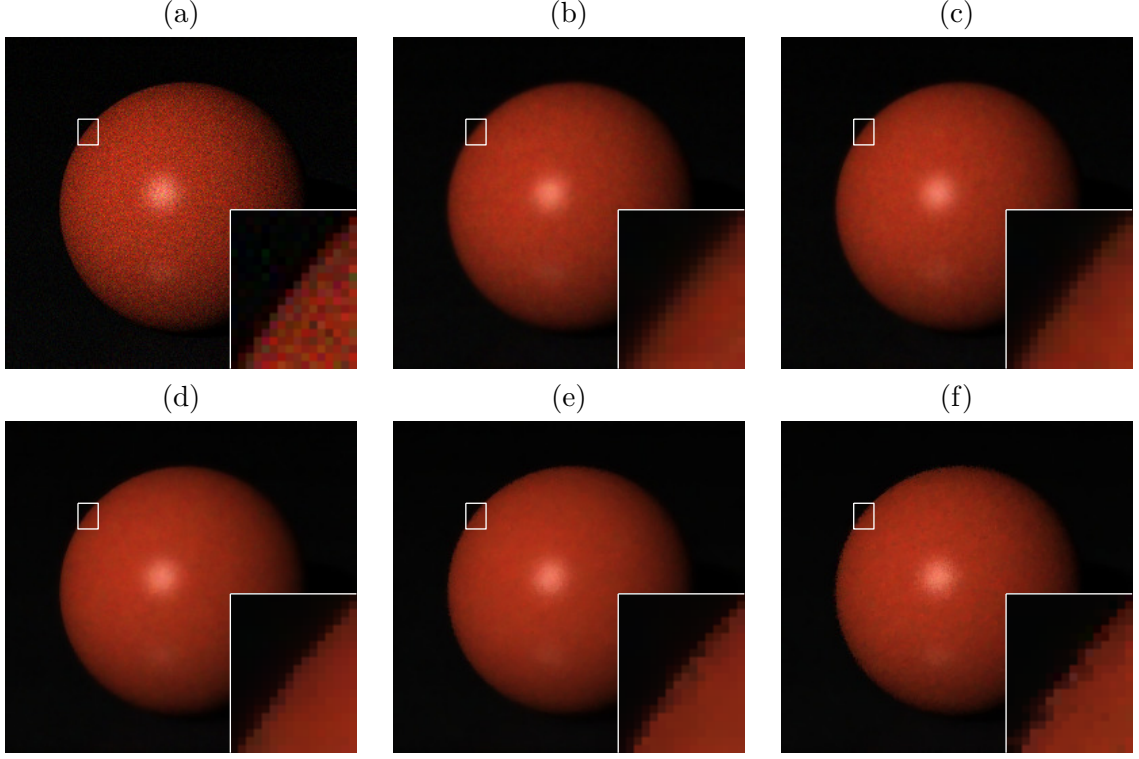


Figure 14: (Effect of α with $\beta = 0$.) The image is corrupted by the Poisson noise with $P = 100$. (a) is the noisy image. (b)-(f) show denoised images with (b) $\alpha = 10^{-1}, \eta = 2$, (c) $\alpha = 10^{-2}, \eta = 2$, (d) $\alpha = 10^{-3}, \eta = 4$, (e) $\alpha = 10^{-4}, \eta = 8$ and (f) $\alpha = 10^{-5}, \eta = 10$.

plot of the zoomed region of the denoised image with $\beta = 0$ and $\beta = 0.005$. The rendered surface of the result with $\beta = 0.005$ is indeed much smoother. The evolution of the energy are shown in the third row of Figure 15. The color elastica term helps the energy to achieve the minimum faster. With non-zero β , the energy of all experiments achieve the minimum within 80 iterations, while with $\beta = 0$, it takes nearly 150 iterations for the energy to achieve its minimum.

6.5 A alternative method to denoise images with color elastica

The second integral in (8) is a fidelity term to guarantee \mathbf{u} is not too far from \mathbf{f} . An alternative way to achieve that is to minimize

$$\int_{\Omega} \left[1 + \beta \sum_{k=1}^3 |\Delta_g v_k|^2 \right] \sqrt{g} d\mathbf{x}, \quad (64)$$

using the Euler-Lagrange as a gradient descent process, until some distance which is proportional to the estimated variance of the noise from the given image is reached. Assume we can estimate the variance of the noise in f : $SD^2 = \text{var}(f - f_0)$, where var denotes the variance of its argument and f_0 denotes the clean image. We would like to find an image by minimizing (64) such that $\text{var}(u - f) \approx SD^2$. Suppose we start with \mathbf{f} , and use an iterative method to minimize (64) such that (64) decreases at each iteration. Denoted the result after the n -th iteration by u^n . One natural criteria to stop iterating is $\text{var}(u^n - f) \geq SD^2$. We demonstrate this method for Gaussian noise with $SD = 0.03$. Note, that the first two fractional steps (26)-(27) in the proposed method is an iterative method to minimize (64), which is an approximation of the gradient decent method. We use (26)-(27) to update $\mathbf{p}^n, \boldsymbol{\lambda}^n, \mathbf{G}^n, g^n$ and compute the denoised image \mathbf{u}^n by solving (14) with $\mathbf{q} = \mathbf{p}^n$ and periodic boundary condition after each iteration. The

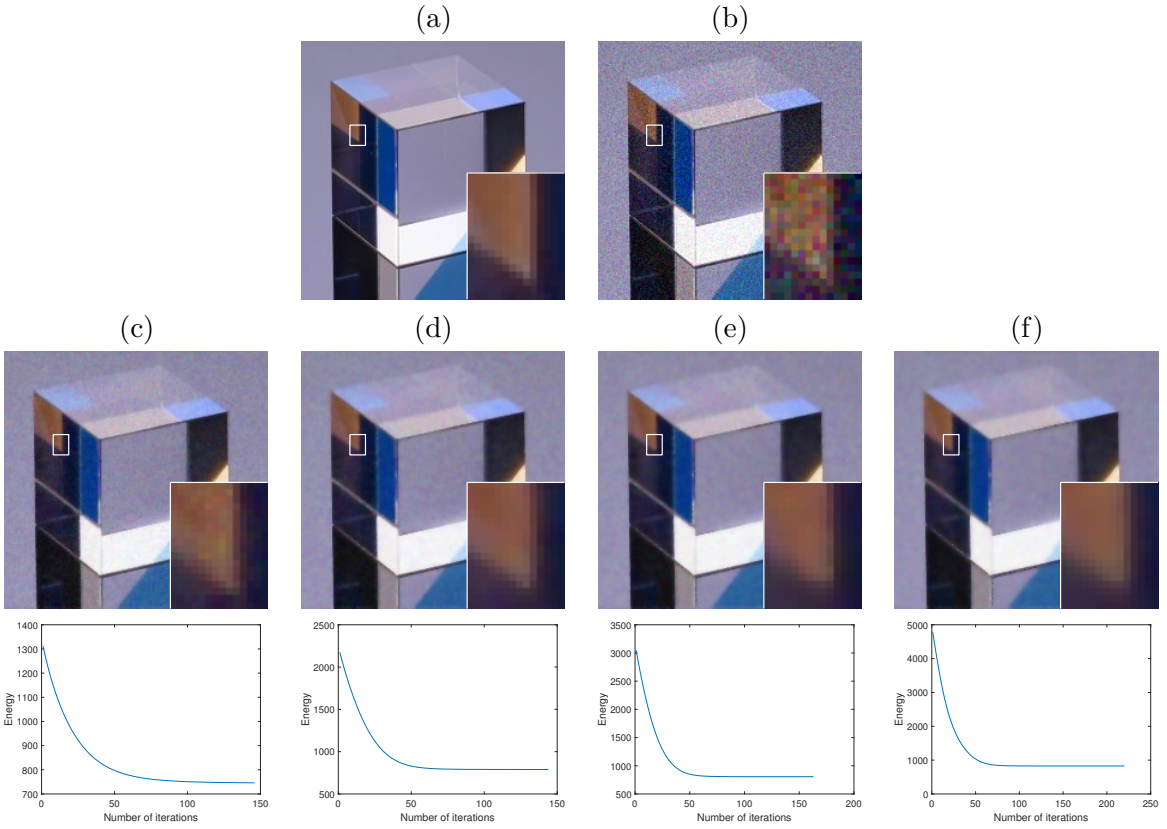


Figure 15: (Effect of β , $\alpha = 0.01, \eta = 1$.) The image is corrupted by the Gaussian noise with $SD = 0.06$. (a) is the clean image. (b) is the noisy image. (c)-(f) show denoised images and the evolution of the energy with (c) $\beta = 0$, (d) $\beta = 0.005$, (e) $\beta = 0.01$, (f) $\beta = 0.02$.

noisy and denoised images are shown in Figure 17. The images are effectively and selectively smoothed. However, the results are not as good as that of (8) shown in Figure 1.

7 Conclusion

We proposed a color elastica model (8), which incorporates the Polyakov action and the squared magnitude of mean curvature of the image treated as a two dimensional manifold in spacial-color space, to regularize color images. The proposed model is a geometric extension of the elastica model (2): when applied to greyscale images, it reduces to a variant of the Euler elastica model. We also proposed an operator-splitting method to solve (8). The proposed method is efficient and robust with respect to parameter choices. The effectiveness of the proposed model and the efficiency of the numerical method are demonstrated by several experiments in color image regularization. The mean curvature term helps to better smooth noisy almost uniform (yet with some color changes) regions in images while keeping the edges sharp.

References

- [1] E. Bae, J. Shi, and X.-C. Tai. Graph cuts for curvature based image denoising. *IEEE Transactions on Image processing*, 20(5):1199–1210, 2010.
- [2] E. Bae, X.-C. Tai, and W. Zhu. Augmented lagrangian method for an euler’s elastica based segmentation model that promotes convex contours. *Inverse Problems & Imaging*, 11(1):1–23, 2017.

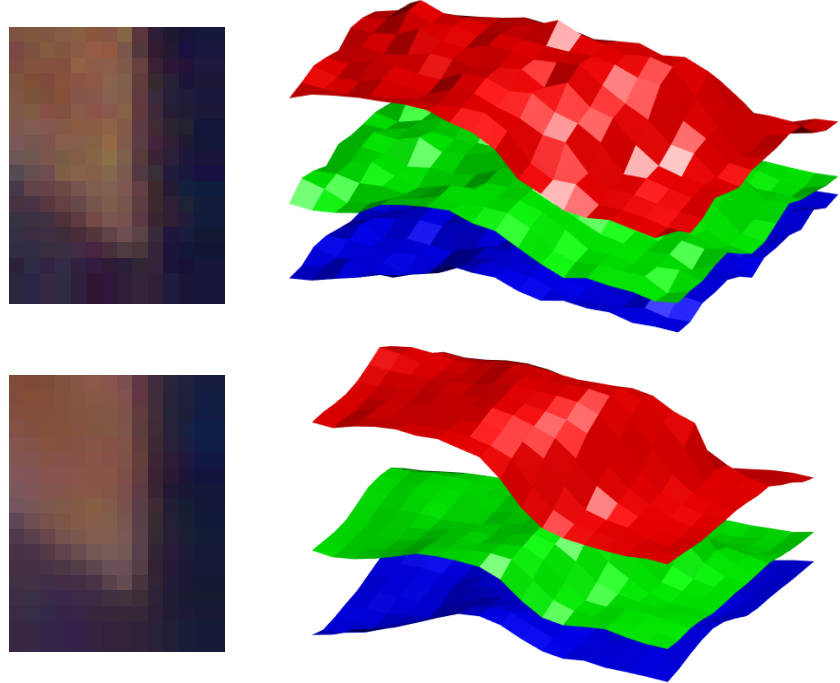


Figure 16: (Effect of β , surface plot.) Comparison of the surface plot of results in Figure 15 (c) and (d). Left: zoomed region of the denoised image in Figure 15 with (first row) $\beta = 0$ and (second row) $\beta = 0.005$. Right: the surface plot of the left images. The RGB channels correspond to the red, green and blue surface, respectively.

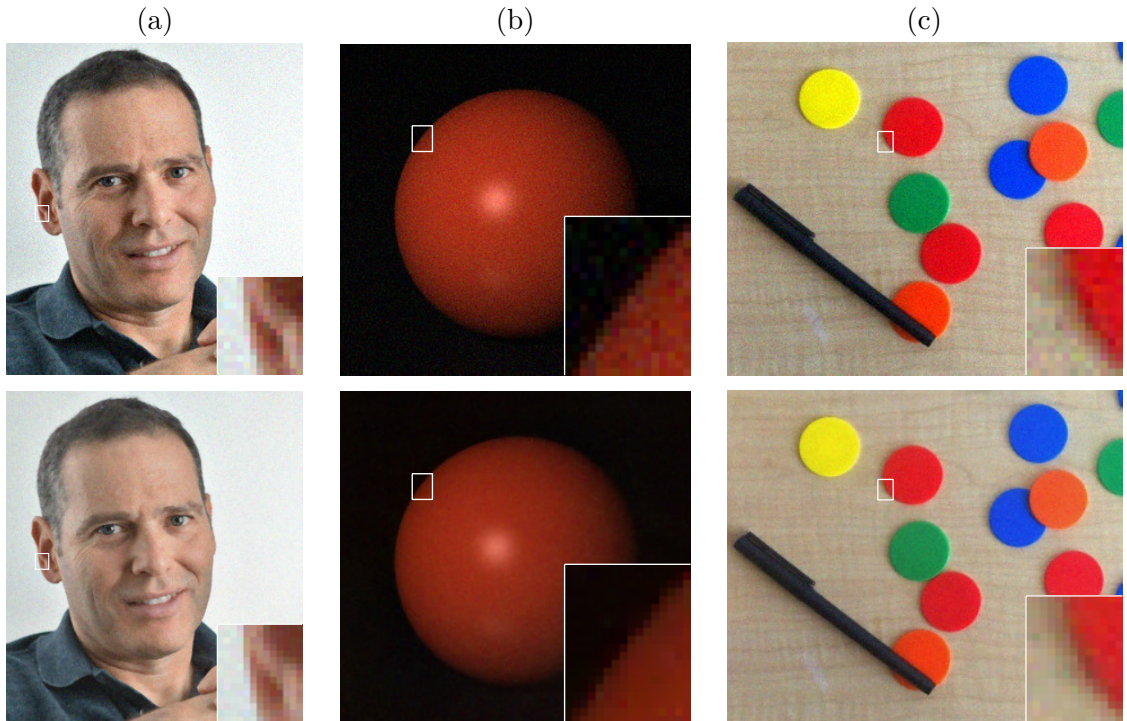


Figure 17: (Model (64), Gaussian noise with $SD = 0.03$. $\alpha = 0.01, \eta = 0.5$.) Image denoising by scheme (26)-(27) on (a) the portrait, (b) the orange ball and (c) chips. The first row shows noisy images. The second row shows denoised images. $\beta = 0.01$ is used for the orange ball, and $\beta = 0.005$ is used for the portrait and chips. The stopping criteria is $\text{var}(u^n - f) \geq SD^2$.

- [3] L. Bar, A. Brook, N. Sochen, and N. Kiryati. Deblurring of color images corrupted by impulsive noise. *IEEE Transactions on Image Processing*, 16(4):1101–1111, 2007.
- [4] T. Batard and M. Bertalmío. On covariant derivatives and their applications to image regularization. *SIAM Journal on Imaging Sciences*, 7(4):2393–2422, 2014.
- [5] P. Blomgren and T. F. Chan. Color tv: total variation methods for restoration of vector-valued images. *IEEE transactions on image processing*, 7(3):304–309, 1998.
- [6] X. Bresson, P. Vandergheynst, and J.-P. Thiran. Multiscale active contours. *International Journal of Computer Vision*, 70(3):197–211, 2006.
- [7] K. Dabov, A. Foi, V. Katkovnik, and K. Egiazarian. Image denoising by sparse 3-d transform-domain collaborative filtering. *IEEE Transactions on image processing*, 16(8):2080–2095, 2007.
- [8] L.-J. Deng, R. Glowinski, and X.-C. Tai. A new operator splitting method for the euler elastica model for image smoothing. *SIAM Journal on Imaging Sciences*, 12(2):1190–1230, 2019.
- [9] S. Di Zenzo. A note on the gradient of a multi-image. *Computer vision, graphics, and image processing*, 33(1):116–125, 1986.
- [10] Y. Duan, W. Huang, J. Zhou, H. Chang, and T. Zeng. A two-stage image segmentation method using euler’s elastica regularized mumford-shah model. In *2014 22nd International Conference on Pattern Recognition*, pages 118–123. IEEE, 2014.
- [11] Y. Duan, Y. Wang, X.-C. Tai, and J. Hahn. A fast augmented lagrangian method for euler’s elastica model. In *International Conference on Scale Space and Variational Methods in Computer Vision*, pages 144–156. Springer, 2011.
- [12] S. Esedoglu and R. March. Segmentation with depth but without detecting junctions. *Journal of Mathematical Imaging and Vision*, 18(1):7–15, 2003.
- [13] R. Glowinski, T.-W. Pan, and X.-C. Tai. Some Facts About Operator-Splitting and Alternating Direction Methods. *Splitting Methods in Communication, Imaging, Science, and Engineering*, pages 19–94, 2017.
- [14] V. Grimm, R. I. McLachlan, D. I. McLaren, G. Quispel, and C. Schönlieb. Discrete gradient methods for solving variational image regularisation models. *Journal of Physics A: Mathematical and Theoretical*, 50(29):295201, 2017.
- [15] K. He, X. Zhang, S. Ren, and J. Sun. Deep residual learning for image recognition. In *Proceedings of the IEEE conference on computer vision and pattern recognition*, pages 770–778, 2016.
- [16] Y. He, S. H. Kang, and H. Liu. Curvature regularized surface reconstruction from point cloud. *arXiv preprint arXiv:2001.07884*, 2020.
- [17] J. Kim, J. Kwon Lee, and K. Mu Lee. Accurate image super-resolution using very deep convolutional networks. In *Proceedings of the IEEE conference on computer vision and pattern recognition*, pages 1646–1654, 2016.
- [18] R. Kimmel, N. Sochen, and R. Malladi. From high energy physics to low level vision. In *International Conference on Scale-Space Theories in Computer Vision*, pages 236–247. Springer, 1997.

- [19] E. Kobler, A. Effland, K. Kunisch, and T. Pock. Total deep variation: A stable regularizer for inverse problems. *arXiv preprint arXiv:2006.08789*, 2020.
- [20] S. Lefkimiatis. Non-local color image denoising with convolutional neural networks. In *Proceedings of the IEEE Conference on Computer Vision and Pattern Recognition*, pages 3587–3596, 2017.
- [21] S. Lefkimiatis. Universal denoising networks: a novel cnn architecture for image denoising. In *Proceedings of the IEEE conference on computer vision and pattern recognition*, pages 3204–3213, 2018.
- [22] M. Nitzberg, D. Mumford, and T. Shiota. *Filtering, segmentation and depth*, volume 662. Springer, 1993.
- [23] A. M. Polyakov. Quantum geometry of bosonic strings. In *Supergravities in Diverse Dimensions: Commentary and Reprints (In 2 Volumes)*, pages 1197–1200. World Scientific, 1989.
- [24] G. Rosman, L. Dascal, A. Sidi, and R. Kimmel. Efficient beltrami image filtering via vector extrapolation methods. *SIAM Journal on Imaging Sciences*, 2(3):858–878, 2009.
- [25] G. Rosman, L. Dascal, X.-C. Tai, and R. Kimmel. On semi-implicit splitting schemes for the beltrami color image filtering. *Journal of Mathematical Imaging and Vision*, 40(2):199–213, 2011.
- [26] G. Rosman, X.-C. Tai, L. Dascal, and R. Kimmel. Polyakov action minimization for efficient color image processing. In *European Conference on Computer Vision*, pages 50–61. Springer, 2010.
- [27] G. Sapiro and D. L. Ringach. Anisotropic diffusion of multivalued images with applications to color filtering. *IEEE transactions on image processing*, 5(11):1582–1586, 1996.
- [28] J. Shen, S. H. Kang, and T. F. Chan. Euler’s elastica and curvature-based inpainting. *SIAM journal on Applied Mathematics*, 63(2):564–592, 2003.
- [29] N. Sochen, R. Kimmel, and R. Malladi. A general framework for low level vision. *IEEE transactions on image processing*, 7(3):310–318, 1998.
- [30] A. Spira, R. Kimmel, and N. Sochen. A short-time beltrami kernel for smoothing images and manifolds. *IEEE Transactions on Image Processing*, 16(6):1628–1636, 2007.
- [31] X.-C. Tai, J. Hahn, and G. J. Chung. A fast algorithm for euler’s elastica model using augmented lagrangian method. *SIAM Journal on Imaging Sciences*, 4(1):313–344, 2011.
- [32] L. Tan, W. Liu, and Z. Pan. Color image restoration and inpainting via multi-channel total curvature. *Applied Mathematical Modelling*, 61:280–299, 2018.
- [33] D. Tschumperle and R. Deriche. Vector-valued image regularization with pdes: A common framework for different applications. *IEEE transactions on pattern analysis and machine intelligence*, 27(4):506–517, 2005.
- [34] Z. Wang, J. Zhu, F. Yan, and M. Xie. Fidelity-beltrami-sparsity model for inverse problems in multichannel image processing. *SIAM Journal on Imaging Sciences*, 6(4):2685–2713, 2013.
- [35] D. Yang and J. Sun. Bm3d-net: A convolutional neural network for transform-domain collaborative filtering. *IEEE Signal Processing Letters*, 25(1):55–59, 2017.

- [36] M. Yashtini and S. H. Kang. A fast relaxed normal two split method and an effective weighted tv approach for euler's elastica image inpainting. *SIAM Journal on Imaging Sciences*, 9(4):1552–1581, 2016.
- [37] J. Zhang and K. Chen. A new augmented lagrangian primal dual algorithm for elastica regularization. *Journal of Algorithms & Computational Technology*, 10(4):325–338, 2016.
- [38] J. Zhang, R. Chen, C. Deng, and S. Wang. Fast linearized augmented lagrangian method for euler's elastica model. *Numerical Mathematics: Theory, Methods and Applications*, 10(1):98–115, 2017.
- [39] K. Zhang, W. Zuo, and L. Zhang. Ffdnet: Toward a fast and flexible solution for cnn-based image denoising. *IEEE Transactions on Image Processing*, 27:4608–4622, 2018.
- [40] W. Zhu, T. Chan, and S. Esedo ḡ lu. Segmentation with depth: A level set approach. *SIAM journal on scientific computing*, 28(5):1957–1973, 2006.
- [41] W. Zhu, X.-C. Tai, and T. Chan. Image segmentation using eulers elastica as the regularization. *Journal of scientific computing*, 57(2):414–438, 2013.
- [42] D. Zosso and A. Bustin. A primal-dual projected gradient algorithm for efficient beltrami regularization. *Computer Vision and Image Understanding*, pages 14–52, 2014.